Brown University
Department of Chemistry & Department of Physics

Exfoliation and Characterizations of Matter and Heterostructure Assembly

Heesoo Kim

Submitted in partial fulfillment of the Honors requirements
for the degree of Bachelor of Science in Chemical Physics of
the Diploma of Brown University, April 2019

Abstract

In this thesis, thicknesses of graphite and BN measured by atomic force microscopy (AFM) was plotted against the optical percentage differences between flakes and the background SiO_2 substrate to achieve a linear relationship between green optical values and AFM thicknesses for BN and between red optical values and AFM thicknesses for graphite. The green linear plot of BN was then used to estimate thicknesses of $RuCl_3$ flakes, which were then plotted against the AFM measurements of the flakes to obtain a linear relationship of slope approximately 1. Using these thickness characterizations, two structures were constructed using the mechanical transfer method: WSe_2-bilayer graphene, and $RuCl_3$-bilayer graphene. WSe_2 was placed in contact with bilayer graphene to measure proximity effect induced spin orbit coupling strength in graphene by observing shifts in the boundaries of a phase diagram, as well as to potentially measure quantum spin Hall effect should the induced spin orbit coupling strength be sufficiently strong. $RuCl_3$ was placed in contact with bilayer graphene for two purposes: 1) observe thermal Hall effect in $RuCl_3$ using graphene as a thermometer, and 2) observe quantum spin liquid phase in $RuCl_3$ by observing a proximity effect in graphene.

Acknowledgements

I would like to express my immense gratitude to:

- Dr. Leo Li, for giving me great guidance throughout the entirety of the senior thesis,
- Dr. Kemp Plumb, for helping me clean up the thesis and for his help in learning about quantum spin liquids,
- my lab members, who were helped me in talking through ideas,
- Department of Physics, for giving me the academic support for completing my thesis,
- and my family and friends, who have put up with me despite me disappearing into the lab for many long hours.

Dedication

To my family, my friends, and my four life-changing years at Brown.

Contents

Chapter 1

Background Theory

This thesis is broadly in two parts–1) exfoliation and characterization of various matters, and 2) constructions of structures composed of matters characterized in part 1 to realize topological insulators.

1.1 Electronic Phases of Matter

In a single, isolated atom, the electrons occupy atomic orbitals with associated discrete energy levels. When two atom placed in contact, the orbitals overlap and the energy levels of electronic states shift to satisfy the quantum mechanics of both atoms. Since electrons are fermions and thus obey the Pauli exclusion principle, a principle that states no two fermions can have the same quantum number, if two identical atoms come in contact with each other, the atomic orbitals of valence electrons–the outermost electrons–split such that the electrons can occupy states of different energy, and the available electrons start to fill the split states starting from states with lowest energy, as depicted in Figure 1.1. Only valence electrons are considered in the band theory because the inner electron orbitals do not overlap significantly enough to produce a wide band, meaning an energy state splits into a very large number of states ($\sim 10^{23}$) to create a continuum.

Crystals are a large number of identical atoms or molecules placed in some periodic structure to form a solid. Along these crystal lattices, the atomic orbitals of the atoms or molecules overlap, and the atomic orbitals split into many discrete molecular orbitals of close but distinct energies, which together forms an energy band (see Figure 1.2). Because these energies are very close to each other compared to the size of the valence band (usually around 23 orders of magnitude smaller than the energy band width), so these energy states can be considered as a continuum [Hol09]. Furthermore, because these valence electrons have multiple possible energy states that can be obtained via excitation, there exists multiple higher energy bands as well that describe the possible excited states.

In a material, the bands of interest are the those nearest to the Fermi level of the material, where a Fermi level of a material is defined as the work needed to add one electron to the material. A state at the Fermi level approximately equal to the chemical potential μ (a good approximation for most metals) has a 50% probability of being occupied by an electron according to the Fermi-Dirac distribution

$$P(E) = \frac{1}{e^{(E-\mu)/kT} + 1} \tag{1.1}$$

where E is the energy of the state, T is the temperature in Kelvin, and k is the Boltzmann constant. The Fermi level does not necessarily have to be an actual energy level. The position of the Fermi level with respect to the highest occupied band determine the type of material such as insulator, semiconductor, or metal.

When the Fermi level lies within a region between the highest fully occupied band and partially occupied bands of a material, the material is called an insulator or a semiconductor. The band immediately below the Fermi level is called the valence band, because that the band is constructed out of the splitting of valence orbitals. For an insulating material at ground state, the valence band is completely filled by electrons. The band immediately above the Fermi level is called the conduction band. The conduction band is constructed out of the first excited energy states of electrons. The gap between the valence and conduction bands is called the band gap. A material

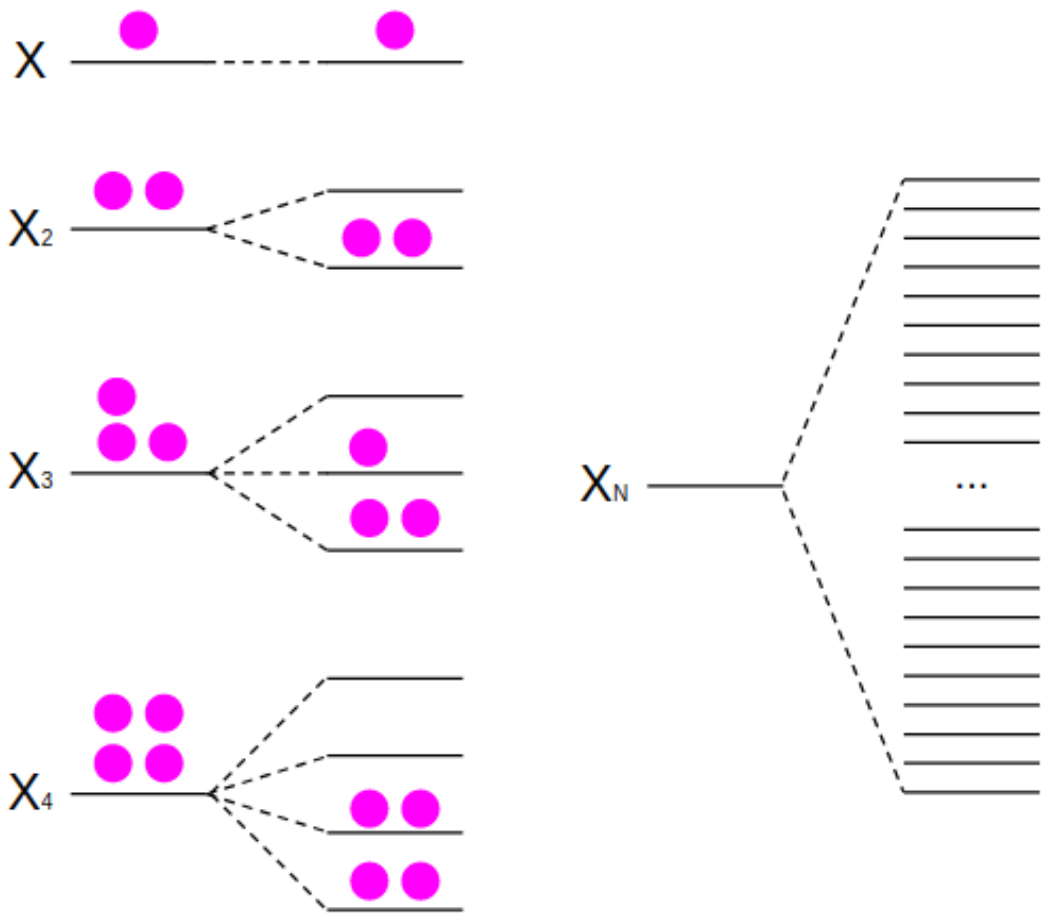

Figure 1.1: When multiple identical atoms are put into contact with each other, the allowed electronic states split around the original energy state to accommodate the electrons without violating the Pauli exclusion principle. Once the energy states are split, the electrons of the participating atoms begin to fill up the energy states starting from those with the lowest energy, as shown by the electrons represented as pink circles. When many atoms are put into contact with each other, such as in solid state materials, the splitting of the energy states become very dense and look to be continuous on the scale of the width of the energy splitting [Hol09].

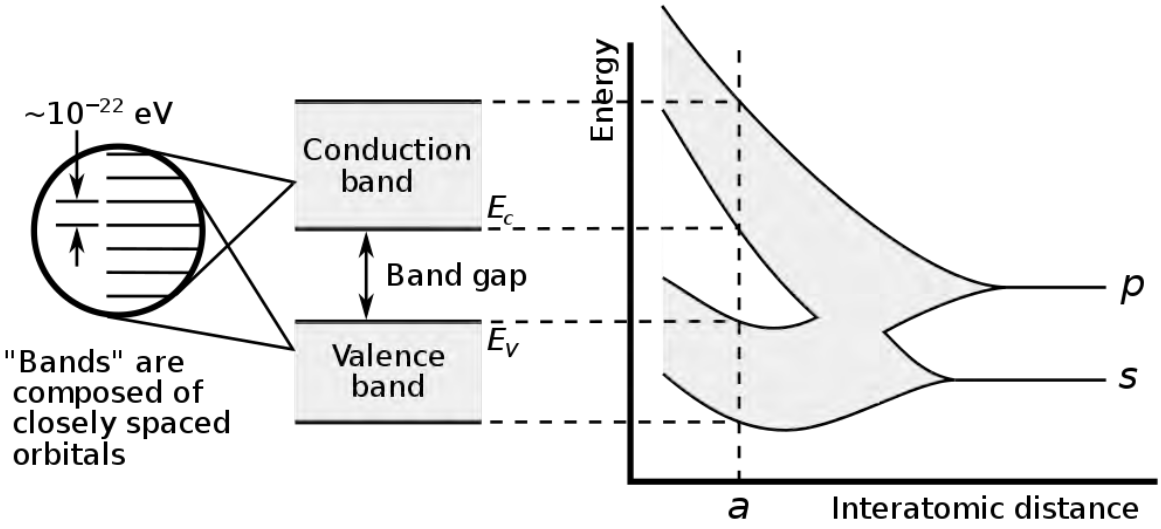

Figure 1.2: Left: The conduction and valence bands are composed of closely spaced discrete energy states that is considered to be continuous due to the differences in the energies of neighboring states being many orders of magnitude smaller than the width of the bands. In a semiconductor or an insulator, there exists a band gap between the valence band (which is filled with the valence electrons when at ground state) and the conduction band (which is empty when the material is at ground state), which denotes the forbidden region where no occupiable electronic energy state exists. Right: The energy bands are plotted as a function of interatomic distance. The valence and conduction bands are composed of s- and p- orbitals, respectively, in this diagram. When atoms are far apart, each of the atoms have identical s- and p- orbitals, as can be observed by a single horizontal line for each of s- and p- orbitals, but as the atoms get very close close, such as at an interatomic distance of a expected of some crystal, a large bandgap appears between the conduction and valence bands, which makes this material an insulator. Source: Wikimedia.

with a small band gap is considered a semiconductor, and a material with a large band gap is considered an insulator.

When the Fermi level lies within a permitted energy band of a material, the material is called a metal or semimetal, and can conduct current. A metal has almost complete overlap between valence and conduction bands, while a semimetal have only a slight overlap.

While metals, semiconductors, and insulators have been studied since 18th century, new classes of materials exhibiting topological nature were only introduced in the 20th and 21st century, and is an active topic of research.

1.2 Topological Insulator

Charges in classical electromagnetism are governed by the Lorentz force

$$\mathbf{F} = q(\mathbf{E} + \mathbf{v} \times \mathbf{B}) \tag{1.2}$$

where $\mathbf{F}$ is the resultant force, q is the charge magnitude, $\mathbf{E}$ is the applied electric field, $\mathbf{v}$ is the velocity of the charge, and $\mathbf{B}$ is the applied magnetic field. In 1879, Edwin Hall showed that when a uniform magnetic field is applied perpendicular to the current, the moving charges are deflected in the direction perpendicular to both the current and the magnetic field, and this accumulation of current on one side of the conductor results in an electric force to counter the magnetic force. Then, a potential difference results perpendicular to the direction of current and magnetic field, called the Hall voltage, which is proportional to the Hall conductance[Hal79]. This Hall conductance is considered to be classical because the Hall voltages may take on continuous values. In 1980, Kalus von Klitzing showed the quantization of classical Hall conductance into integer multiples of e^2/h, where e is the charge of electron and h is the Planck's constant, when a two-dimensional electron gas in low temperatures is subjected to a strong perpendicular magnetic

field [vKDP80], confirming the 1975 predictions of Ando *et al.* [AMU75]. These Hall conductances can be considered as conducting edge states (see the leftmost diagram in Figure 1.3). These quantum Hall edge states were shown by Halperin in 1982 to be stable against local perturbations, which relates to the topological nature of these states.

In 2004, a spin Hall effect was observed by Kato *et al.* in semiconductors [KMGA04]. A spin Hall effect, originally predicted in 1971 by Dyakonov and Perel, is a spin accumulation along the lateral surfaces of some conducting material (much like the classical Hall effect in which charges build up along the boundaries) such that the spins on the same surface are of same direction, and spins of opposite surfaces are of opposite directions [DP71b] [DP71a]. Unlike the classical Hall effect, no external magnetic field is necessary to obtain the spin Hall effect because the current itself creates a magnetic field. In 2007, König *et al.* experimentally realized a quantum spin Hall effect in HgTe sandwiched between two sheets of CdTe to form quantum wells [KWB$^+$07], a system which was first proposed in 1987 by Pankratov, Pakhomov, and Volkov as being one that may support a quantum spin Hall state, which was first developed by Kane and Mele in 2005 [KM05a] by building on the graphene model of integer quantum Hall effect (the integer being quantization of Hall effect into integer multiples of e^2/h rather than some fractional multiples) realized by Haldane in 1988 [HR88]. Similar to the classical spin Hall effect, a quantum spin Hall effect needs no external magnetic field to realize the spin build up according to the spin parity (see the middle diagram of Figure 1.3).

While this thesis focuses mostly on the quantum spin Hall effect and the experimental realizations of the effect, other topological materials have since emerged, such as the quantum anomalous Hall effect that is the quantum cousin the the anomalous Hall effect first measured in 1881. The anomalous Hall effect is named as such because the Hall effect in ferromagnetic materials is governed by the magnetization of the material, needs no external magnetic field, and is much greater than ordinary Hall effect [Hal81]. In a quantum anomalous Hall effect, first measured in 2013 by Xue Qikun *et al.*, the anomalous Hall conductance quantizes into integer multiples of e^2/h, much

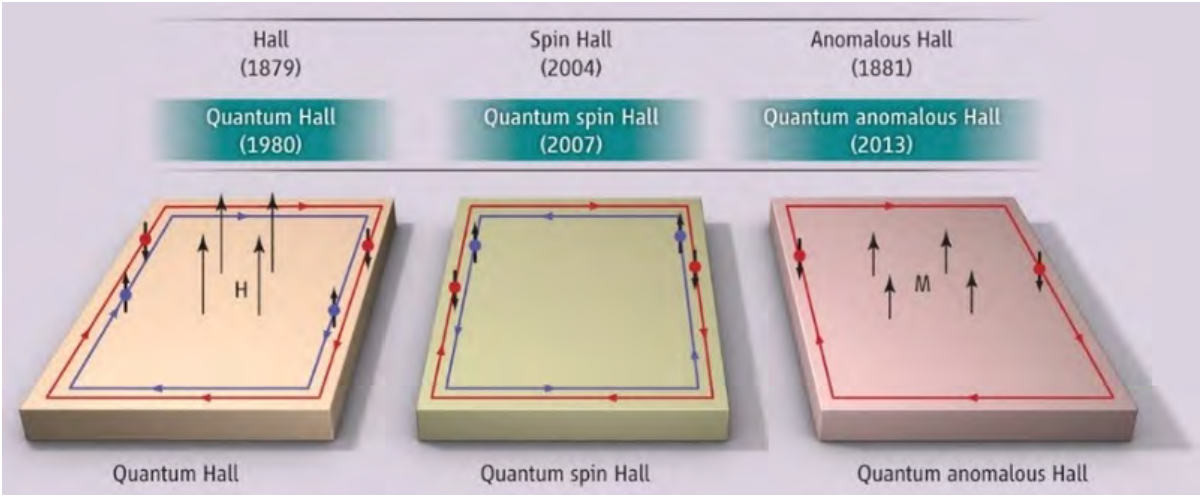

Figure 1.3: Left: In a quantum Hall state, the magnetic field is applied perpendicular to the current flow to produce dissipationless current flow with no backscattering. Because current may only flow in a single direction, quantum Hall state produces chiral edge current, with the direction determined by the direction of the applied magnetic field. Middle: In quantum spin Hall state, no magnetic field is applied to the system, and spin accumulates along either side of the current flow, with only spins of same direction accumulating on same sides, and spins of opposite directions accumulating on opposite sides. Right: In a quantum anomalous Hall effect, no external magnetic field is imposed on the system, but the system generates its own magnetic field due to the ferromagnetic or ferrimagnetic nature of the material. Because the direction of the magnetization is intrinsic to the material, dissipationless currents of only a single direction can be achieved along the edge.

like the ordinary quantum Hall effect [CZF$^+$13]. However, these integers correspond to the Chern number, which is a number topologically characteristic of a material band structure [Van18] (see the rightmost diagram of Figure 1.3). Due to the quantization of anomalous Hall conductance into Chern number multiples of the conductance quantum, the quantum anomalous Hall insulators are also called Chern insulators.

A topological insulator is a quantum spin hall system that exhibits insulating bulk but conducting edge states [KM05a]. Because charge carriers cannot backscatter due to helical spin-momentum locking of edge states, topological insulators can enable low-power electronics and quantum computing. A material is considered a topological insulator if it has an odd number of band inversions between bands of opposite parity (the opposite parity meaning odd vs. even). An inverted band structure has edge states that continuously connects the valence band and the conduction band in contrast to a normal band structure in which edge states only connect the conduction band to

itself (see Figure 1.4). Because the edge states continuously connect between valence and conduction band, the bulk is insulating, but the edge states become conducting. These edge states are topologically protected via time-reversal symmetry, and can only be destroyed by applied magnetic field (which destroys the time-reversal symmetry). A time-reversal symmetry refers to the conservation of entropy (a measure of disorder in a system), and topologically protects edge states through Kramer's theorem, which states the eigenstates of time-reversal invariant Hamiltonians must be at least two-fold degenerate. Time reversal is represented by the anti-unitary operator T

$$T = e^{i\pi S_y/\hbar}K \tag{1.3}$$

where S_y is the spin operator and K is the complex conjugation. Because $T^2 = -1$ for spin 1/2 electrons, the Kramer's theorem, which states that a Hamiltonian invariant under time reversal operator must have eigenenergies that are at least twofold degenerate at points mirror symmetric about zero momentum, and these degenerate points are called Kramer doublets [Van18].

A band inversion occurs when the conduction band and valence band overlaps by some small amount, and spin-orbit coupling (SOC) produces a gap between the conduction and valence band by inverting the order of conduction and valence bands at the overlap. The opening of gap going from semimetal to topological insulator can be achieved by strong SOC, as shown by Kane and Mele in 2005, but the challenge lies in identifying materials or some heterostructures–a structure made of two-dimensional materials stacked in some order to exploits interactions between the materials–that exhibit sufficiently strong SOC, as the size of the gap is proportional to the strength of the SOC [KM05a]. This thesis partially focuses on the construction of heterostructures that are expected to exhibit a strong SOC that may open an inverted band gap and thus could be topological insulators.

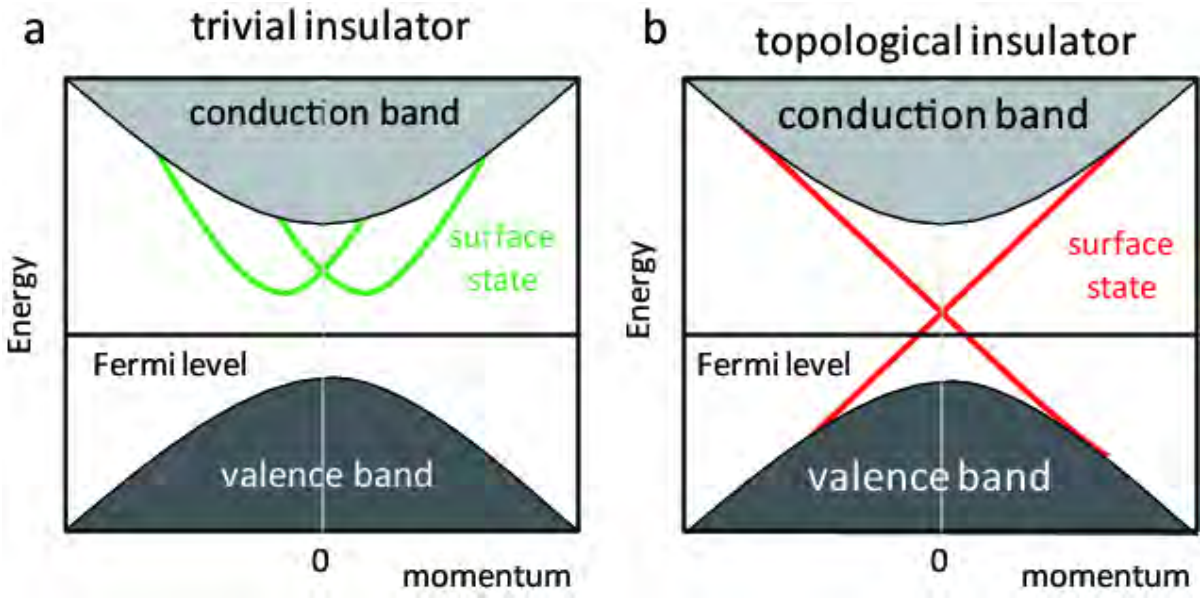

Figure 1.4: (a) A topologically trivial insulator, like all insulators, have conduction and valence bands separated by an energy gap, and the Fermi level lies in the energy gap. The topologically trivial nature is characterized by the surface states (or edge states) connecting only from conduction band to conduction band, and thus can be continuously retracted into a single point. (b) In a topologically nontrivial insulator, while the conduction and valence bands are still separated by a bandgap and contains the Fermi level within its bandgap, the surface states (or edge states) connect conduction band to valence band, crossing at momentum of 0, and cannot be continuously retracted into a single point.

1.3 Recent Experimental Realizations of Quantum Spin Hall State

A few experimental efforts have attempted to induce counter-propagating edge states with topological protection in graphene heterostructure in the quantum Hall effect regime [YSYH$^+$14, SYLY$^+$17]. Ref. [YSYH$^+$14] designed a clever experiment by applying a large parallel magnetic field while tuning monolayer graphene (MLG) to be at half-filling of the lowest Landau level (LLL), $\nu = 0$. Since the LLL in MLG is four-fold degenerate with spin and valley isospin degeneracy, as parallel magnetic field stabilizes a spin polarized ground state at $\nu = 0$, the filled and empty LL are necessarily valley unpolarized. The resulting band structure is shown in Fig. 1.5, while the system is insulating away from sample edge, two valley branches above and below the Fermi surface disperse in opposite directions near sample edge, giving rise to counter-propagating edge modes with opposite spin-polarization. This is essentially the same edge configuration as the famous quantum spin Hall phenomena proposed by Ref. [KM05b], but the band inversion is induced by manipulating the symmetry of the $\nu = 0$ state in MLG, instead of SOC effect.

Ref. [SYLY$^+$17] used a different approach. It was demonstrated that when two graphene layers were assembled with a large twist angle, the ground state in each layer is largely decoupled from the other, as if electrons are confined within each layer with layer being a good quantum number. In such a structure, two graphene layers can be tuned to $\nu = 1$ and -1 with electro-static gating, giving rise two edge modes with opposite chirality and opposite spin polarization, which is similar to the structure of QSH state. In this case, topological protection derives from the fact that $\nu = 1$ and -1 edge have opposite spin polarization, and the fact that two graphene layers are decoupled due to the twist angle.

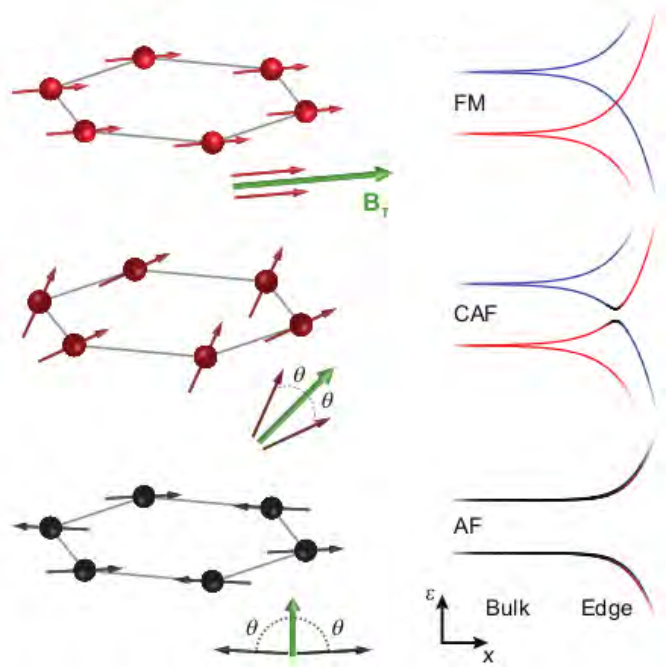

Figure 1.5: At the regular antiferromagnetic order (bottom), the conduction and valence bands of the edge remain separated. However, at very strong transverse magnetic field, the edge bands split, resulting in a band inversion with half of the valence band and half of the conduction band, as shown in the top figure.

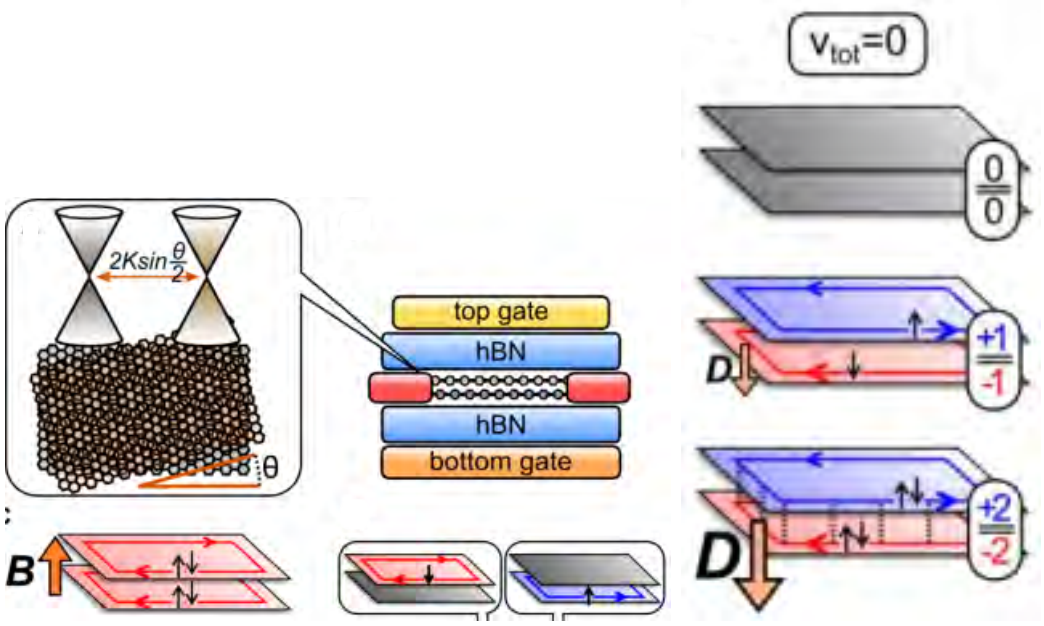

Figure 1.6: Decoupled bilayer graphene exhibiting quantum Hall effect of opposite chirality put together to exhibit an approximation of quantum spin Hall effect.

1.4 Magnetic States of Matter

Materials can be broadly classified into five states based on their magnetic behaviors: 1) diamagnetic, 2) paramagnetic, 3) ferromagnetic, 4) ferrimagnetic, and 5) antiferromagnetic materials. Diamagnetic and paramagnetic materials are not magnetically ordered, while ferromagnetic, ferrimagnetic, and antiferromagnetic materials exhibit long-range magnetic order at temperatures below some critical temperature characteristic of the materials.

All materials have associated magnetic susceptibility, which is a dimensionless constant that describes the degree of magnetization of a material under an applied magnetic field. The magnetic susceptibility, χ, is governed by the Equation 1.4,

$$\mathbf{M} = \chi \mathbf{H} \tag{1.4}$$

where $\mathbf{M}$ is the magnetization of the material (magnetic dipole moment per unit volume) and $\mathbf{H}$ is the applied magnetic field strength. A magnetic dipole moment is magnetic strength and orientation that is caused by intrinsic spin and electric charge of electrons, and produces a magnetic field. A diamagnetic material has a negative magnetic susceptibility, and is composed of atoms with that have completely filled orbital shells and thus have no unpaired electrons [Blu01]. When a diamagnetic material is exposed to a magnetic field, a magnetic moment opposing the magnetic field is induced, but under zero magnetic field, the material has no magnetization. The magnetic susceptibilities of diamagnetic materials are largely temperature independent.

Paramagnetic materials are composed of atoms with a net magnetic moment as a result of unpaired electrons. Without external magnetic field, paramagnetic material has no magnetization because the magnetic moments of atoms with unpaired electrons point randomly and cancels out when observed in bulk (see Figure 1.7a). Paramagnetic materials have positive susceptibility because applied magnetic field can encourage the magnetic moments of atoms with unpaired electrons to line up in a particular direction, but higher temperature encourages disorder in the directions of

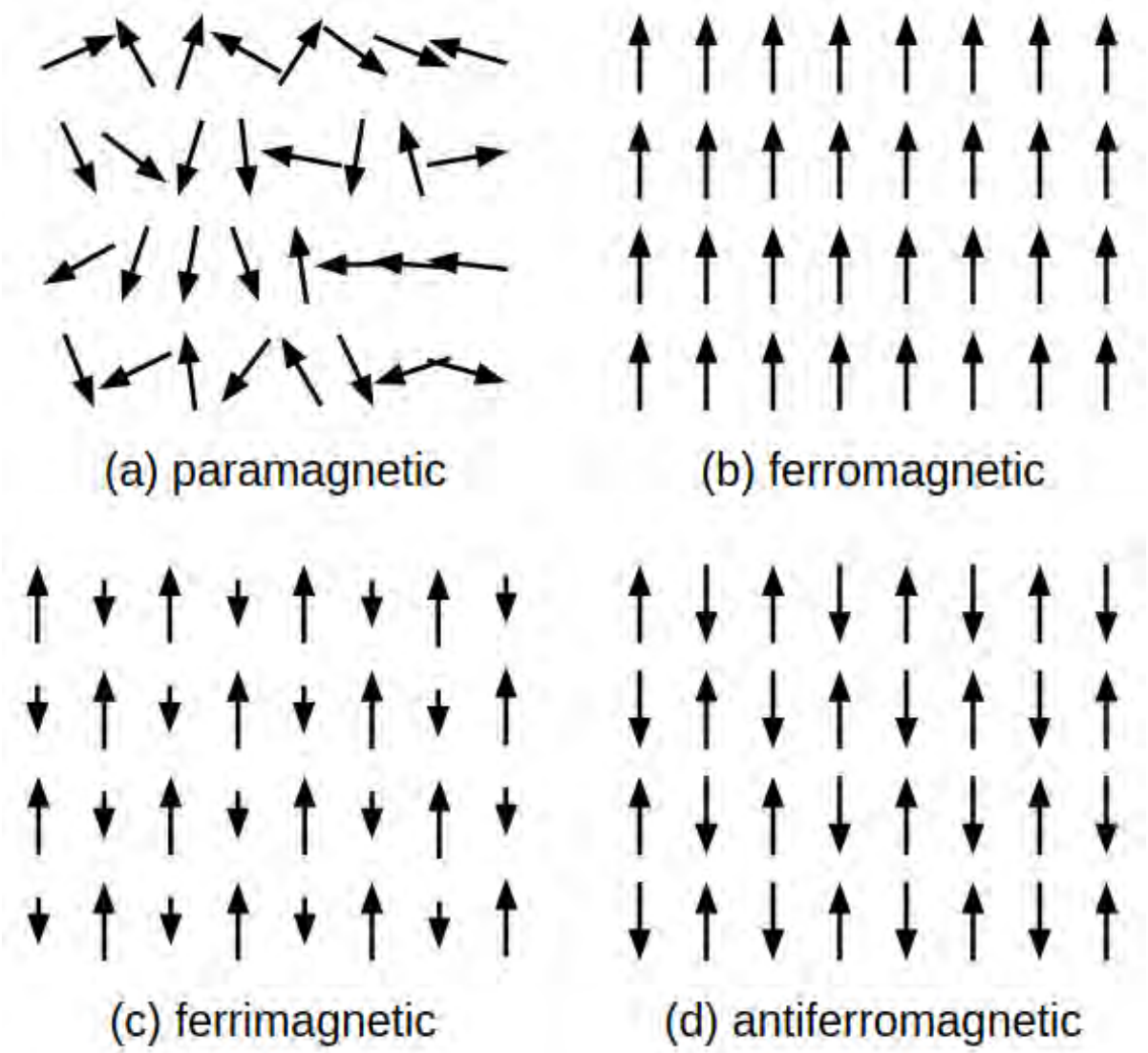

Figure 1.7: (a) A paramgnetic material has atoms exhibiting individual magnetic dipole moments, as represented by the individual arrows, but the magnetic dipole moment of an atom does not interact with the magnetic dipole moments of the neighboring atoms , so the the individual dipole moments point randomly in space and results in a net zero magnetization of the material. (b) A ferromagnetic material has interacting individual magnetic dipole moments, and this intra-atomic interaction of dipole moments result in a spontaneous ordering of the magnetic moments such that the magnetic moments point in the same direction and thus manifests as a net magnetization of the material. (c) A ferrimagnetic material also has interacting individual magnetic dipole moments and thus have spontaneous ordering of the magnetic moments, but the spins are ordered antiparallel to each other, and the magnitude of the antiparallel magnetic moments are unequal in strength, so the material as a nonzero net magnetization. (d) An antiferromagnetic material has interacting individual magnetic dipole moments resulting in a spontaneous antiparallel ordering of the magnetic moments, and because the antiparallel magnetic moments are of equal strength, the net magnetization of the material is zero.

magnetic moments [MFT14].

Ferromagnetic materials show spontaneous ordering of magnetic moments along the same direction (see Figure 1.7b) even without external magnetic fields because the magnetic moments of the atoms making up the materials strongly interact with neighboring magnetic moments. These interactions result from electronic exchange interactions, which are quantum mechanical effects that occurs between identical particles as a result of Pauli exclusion principle, which states that two electrons cannot have the same quantum numbers. When valence orbitals overlap in multi-atomic systems, the electric charge distributions are more sparse when the electrons are of same spins rather than opposite spins, thus decreasing the electrostatic energy Even though the magnetic moments are strongly interacting and favor parallel alignment, at sufficiently high temperature, the thermal energy overcomes the electronic exchange and randomizes the magnetic moments. The temperature at which this disorder occurs is called the Curie Temperature (T_C), and is an intrinsic property of materials [AM76].

Ferrimagnetic materials also show spontaneous ordering of magnetic moments, but has two populations of atoms with opposite and unequal magnetic moments (see Figure 1.7c), and thus exhibit spontaneous magnetization. Similar to ferromagnetic materials, ferrimagnetic materials also have Curie temperatures above which no magnetic order is observed [AM76].

Antiferromagnetic materials are similar to ferrimagnetic materials in that the material exhibits a spontaneous ordering of magnetic moments with two populations of opposing magnetic moments, except the opposing magnetic moments are of equal magnitude (see Figure 1.7d). Because the opposing magnetic moments are equal, the net magnetic moment of antiferromagnetic materials is zero. Antiferromagnetic materials exhibit the antiferromagnetic order at low temperatures, but no magnetic order is exhibited at temperatures above the Curie temperature and the material becomes paramagnetic [Blu01].

In 1973, Phil Anderson proposed another magnetic state of matter called a quantum spin liquid which preserves disordered spin state even at very low temperatures due to spin frustration inherent

in the crystal lattice as opposed to alignment of magnetic moments favored by strength interactions [And73]. A spin frustration can be described as follows: Consider an equilateral triangle with an antiferromagnetically interacting Ising spins at each vertex, and let us label them as spins A, B, and C. If spin A is pointing up, and spin B is pointing down, then spin C needs to point down to obtain lowest energy with spin A, but also needs to point up to obtain the lowest energy with spin B. The spins in this triangular lattice are frustrated because no ground state satisfy antiferromagnetic order for every spin interaction.

1.5 Quantum Spin Liquid

A quantum spin liquid (QSL) is a phase of matter with interacting quantum spins that has an very high degree of entanglement (i.e. a massive quantum superposition), which results in the preservation of the disorder in its spins even at very low temperatures. While the triangular lattice model discussed above is a good illustration of spin-frustrated systems, finding realistic models for QSL has shown to be a difficult task. To date, the only exactly solvable model of QSL is the Kitaev model [Kit05], which consists of S = 1/2 spins on a honeycomb lattice under nearest neighbor Ising interactions of direction-dependent spin exchange parameters as shown in Figure 1.8. The magnetic Hamiltonian of this model is given by

$$H = -J_{XX} \sum_{XX-links} \sigma_j^X \sigma_k^X - J_{YY} \sum_{YY-links} \sigma_j^Y \sigma_k^Y - J_{ZZ} \sum_{ZZ-links} \sigma_j^Z \sigma_k^Z \tag{1.5}$$

where J_{XX}, J_{YY}, and J_{ZZ} are the bond dependent Ising exchange interactions and σ_j^X is the X spin of vertex j, and similarly for Y and Z spins.

Because Pauli spin matrices do not commute with each other, there exists no ground state that is simultaneously an eigenstate for each of the XX, YY, and ZZ terms, which makes the magnetic spin frustration be inherent in this model, and even at very low temperatures, the spins in the system remains frustrated. Kitaev has an exactly solved solution for this QSL model in which

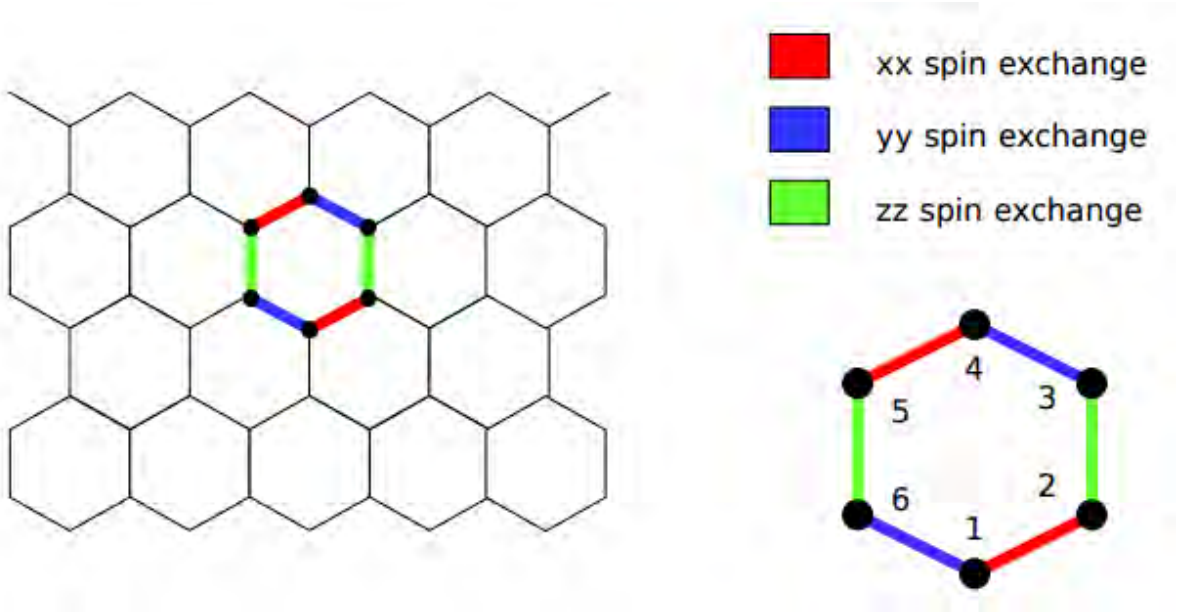

Figure 1.8: Spin-1/2 Kitaev honeycomb lattice with spins located at the vertices. The edges are categorized into three types of links–a XX spin exchange, a YY spin exchange, and a ZZ spin exchange–based on the direction of the link, and thus every unit hexagon is constructed out of 2 XX spin exchanges, 2 YY spin exchanges, and 2 ZZ spin exchanges, much as depicted in this figure.

each spin can be described by four Majorana operators, thus predicting fractional S = 1/2 spins to manifest as Majorana fermions.

A candidate for an approximate Kitaev QSL is ruthenium trichloride (α-$RuCl_3$), which is a layered Mott insulator with an effective total angular momentum $J_{eff} = 1/2$ and a strong SOC [DPY+17]. A Mott insulator is a class of materials that are insulating due to electron-electron interactions despite being predicted to be a conductor within conventional band theories mentioned above. A conventional band theory incorrectly predicts various transition metal oxides to be conductors due to the odd number of electrons per unit cell, which results in partially filled bands. The formation of energy gap between the conduction and valence band is a result of screening between the *3d* electrons. The strong electron-electron interactions allows for a large magnetic spin frustration, making Mott insulators with hexagonal lattices into good candidates for Kitaev QSL. $RuCl_3$ preserves the Ising-type antiferromagnetic order with zigzag spin structure even at low temperatures [DPY+17] [KOM+18a] because while the Hamiltonian of $RuCl_3$ includes Equation 1.5, the $RuCl_3$

Hamiltonian also includes other terms that compete against the frustration to favor an ordering of the magnetic moments. α-$RuCl_3$ is interesting in that despite being an insulator, it exhibits thermal Hall effect in low temperatures in high magnetic fields (7∼8 Tesla), thus begging the question of what allows for heat to be transported when electrons cannot freely flow through the material? The bulk α-$RuCl_3$ is sensitive to stacking faults (defects in crystals that are results of misalignment between layers of the crystal structure), which enhances the antiferromagnetic order, likely due to the exchange interactions being strengthened by the stacking disorder [ZWO+18].

1.6 Recent Experimental Realizations of Quantum Spin Hall State

Thus far, electron transport measurements in QSL are still in infancy, and much of experimental research around Kitaev QSL candidates has primarily revolved around characterization of materials via x-ray diffraction and neutron scattering measurements.

Kasahara *et al.* has shown in 2018 that α-$RuCl_3$ at its spin liquid state exhibits a large positive thermal Hall conductance when subjected to external magnetic field and a temperature gradient. $RuCl_3$ is a good insulator, meaning that little to no mobile charge carriers are present even at room temperature, so no charge carriers are enabling the thermal transport [KOM+18b]. As such, the mechanism of the the large thermal Hall effect observed in $RuCl_3$ can be potentially attributed to mobile Majorana fermions.

Chapter 2

Material Exfoliation and Characterization

2.1 Scotch Tape Exfoliation

2.1.1 Geim and Novoselov's Scotch Tape Preparation [NGM+04]

A bulk crystal of interest of several mm in size was placed on a clean piece of Scotch magic tape, which is folded and torn quickly multiple times until a thin layer of graphite covered a 1.5 cm by 1.5 cm square area of tape. This tape is called the 'mother tape.' From each of the mother tape, two daughter tapes were each exfoliated by covering the graphite surface with magic tape and quickly tearing the tape from the mother tape. This method will here-forth be referred to as the Scotch tape method.

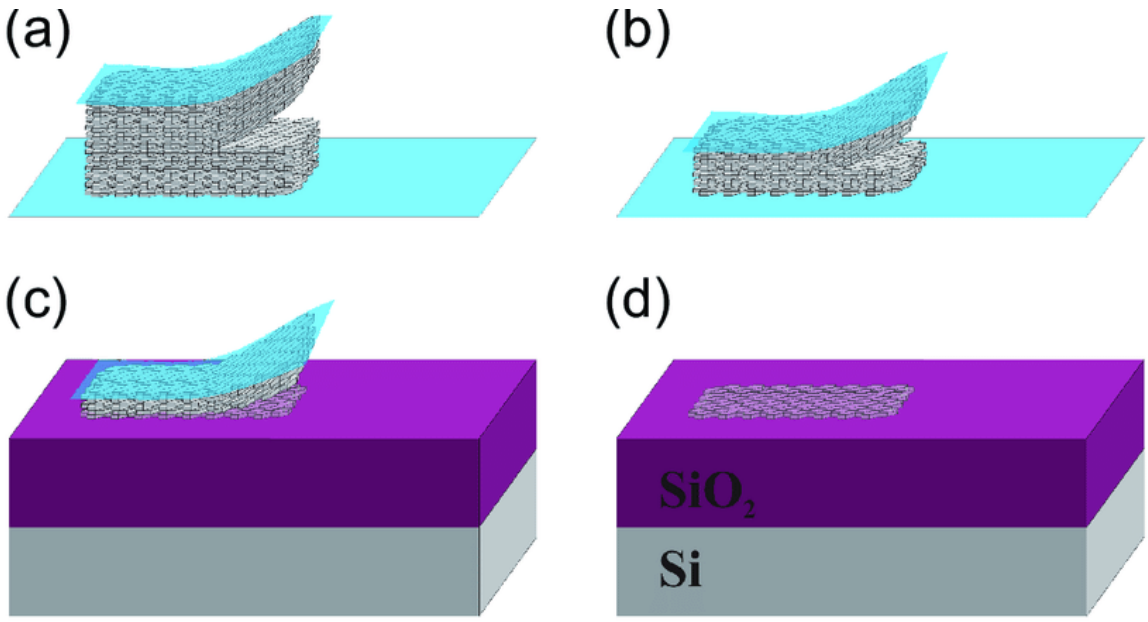

Figure 2.1: Scotch tape exfoliation of 2-dimensional material. Atomic thin layer of 2D material can be obtained using the so-called Scotch tape method. (a)-(b) Bulk crystal of certain material is first placed on a clean Scotch tape. Each time it is pressed into another tape and torn apart, its thickness reduces. (c) After repeating step (a) and (b) a few times, the Scotch tape is pressed onto a SiO_2-Si chip before being torn away, sometimes leaving behind an atomic layer of 2-dimensional material as shown in (d).

2.1.2 Graphite

A tape of thin graphite crystals was prepared using the Scotch tape method, and for each daughter tape, a Si wafer with a dimension of 1.2 cm by 1.2 cm was placed in O_2 plasma for 10 seconds, as depicted in Figure 2.1 a and b. After the plasma treatment, the wafer was covered with a daughter tape, and was baked for 2 minutes at 110°C. After baking, the tape was quickly torn away from the wafer, leaving behind graphite flakes on the wafer.

2.1.3 BN

A tape of thin BN crystals was prepared using the Scotch tape method, taking care to avoid putting pressure directly on the flakes during the folding process to prevent contamination of flake surfaces by tape residue. For each daughter tape, a Si wafer with a dimension of 1.2 cm by 1.2 cm was placed in O_2 plasma for 10 seconds. After the plasma treatment, the wafer was covered with a daughter tape, and was baked for 2 minutes at 110°C. After baking, the tape was torn slowly from the wafer, leaving behind BN flakes on the wafer.

2.1.4 $RuCl_3$

After preparing tapes of $RuCl_3$ using the Scotch tape method, $RuCl_3$ can be exfoliated in two ways: 1) with using O_2 plasma + baking, and 2) without.

For the first method, a Si wafer with a dimension of 1.2 cm by 1.2 cm was placed in O_2 plasma for 10 seconds. After the plasma treatment, the wafer was covered with a daughter tape, and was baked for 2 minutes at 110°C. After baking, the tape was quickly torn from the wafer to leave behind $RuCl_3$ flakes on the wafer.

For the second method, the Si wafer was not treated with O_2 plasma, but was instead immediately covered with the daughter tape. After placing the tape on the wafer, the tape was torn slowly

from the wafer, leaving behind $RuCl_3$ flakes on the wafer.

The first method was found to leave a greater number of flakes as well as more thinner flakes of $RuCl_3$ on the wafer compared to the second method. However, the first method also resulted in dirtier flakes (flakes with foreign matter on the surface) compared to the second method, because the tape would melt on the flakes during the baking process.

$RuCl_3$ is quite brittle, and the exfoliated flakes are mostly shattered. Therefore, while making the mother and daughter tapes, one must be careful not to press down on the flakes directly to avoid shattering the flakes.

2.1.5 WSe_2

WSe_2 was more difficult to exfoliate compared to the other materials. Tapes of WSe_2 were prepared using the Scotch tape method, but instead of creating daughter tapes, the mother tapes were directly used to exfoliate WSe_2 flakes on top of Si wafer. A Si wafer with a dimension of 1.2 cm by 1.2 cm was placed in O_2 plasma for 5 minutes. After the plasma treatment, the wafer was covered with a mother tape, and was baked at 100°C for 3 minutes. After baking, the tape was slowly torn from the wafer to leave behind WSe_2 flakes on the wafer.

2.2 Optical Thickness Estimation

2.2.1 BN Thickness

Pictures of BN flakes labeled with thickness as measured via atomic force microscopy (AFM) was provided by Dr. Li. These flakes was analyzed in terms of Red-Green-Blue (RGB) color composition. The % change in RGB values in flake picture from that of the background Si picture

was calculated using the Equation 2.1,

$$\%change = \frac{background - spot}{background} \tag{2.1}$$

and the AFM-measured thicknesses of the flakes were plotted against this % change. The red and green values showed a strong correlation between the % difference and thickness, with the red % values showing a strong sinusoidal relationship, likely due to the Fabry-Perot nature of the SiO_2 and BN, while the green % values showing a linear relation between the % values and the thickness range of interest.

2.2.2 Graphite Thickness

Similar to BN, the optical data for graphite was also plotted against the thicknesses obtained from AFM measurements taken by Dr. Li. While graphite is a metal and thus show optical saturation at a large thickness, thin graphite flakes still show a linear relation between the optical data and the thickness of the flakes. Even though the points seem to have a large spread, the sources of error are different between the thin-regime and the thick regime. At thickness of $>\sim 2$ nm, AFM measurements are very accurate, but the color characterization has high error. At thickness of $<\sim 2$ nm, such as a monolayer or bilayer graphene, optical measurements show a clear difference between graphenes of different number of layers, but AFM thickness is overwhelmed by the difference in the atomic interaction between the AFM tip and SiO_2 compared to the atomic interaction between the AFM tip and the material of interest such as graphite.

2.2.3 $RuCl_3$ Thickness

The thicknesses of $RuCl_3$ flakes were estimated using the green % linear relation in BN flakes, and were plotted against the AFM thicknesses of the flakes. The thickness of $RuCl_3$ estimated using

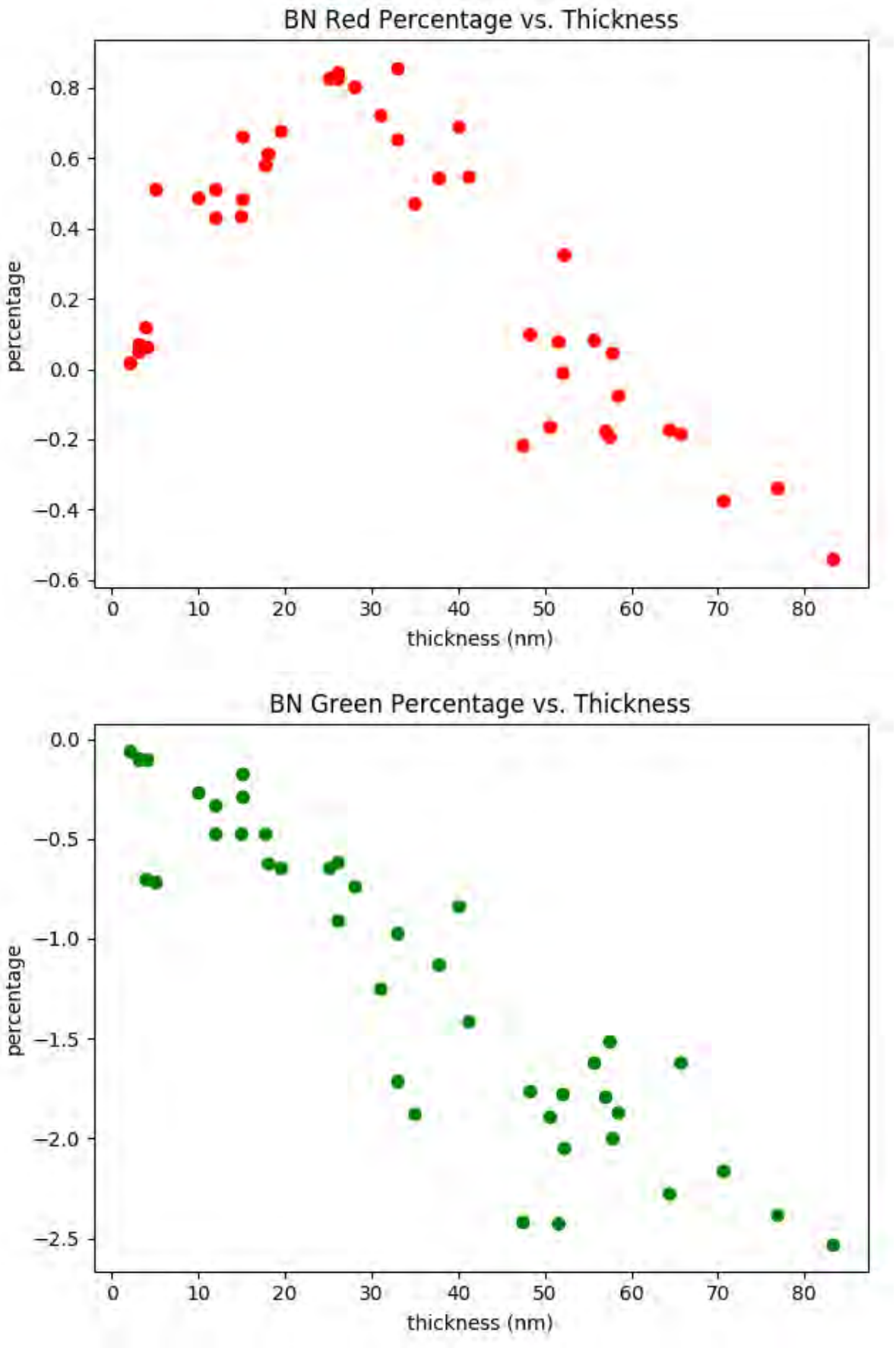

Figure 2.2: Plot of red % difference and blue % difference against AFM thickness for BN. The % difference was calculated by the equation: % diff = (background - flake) / background.

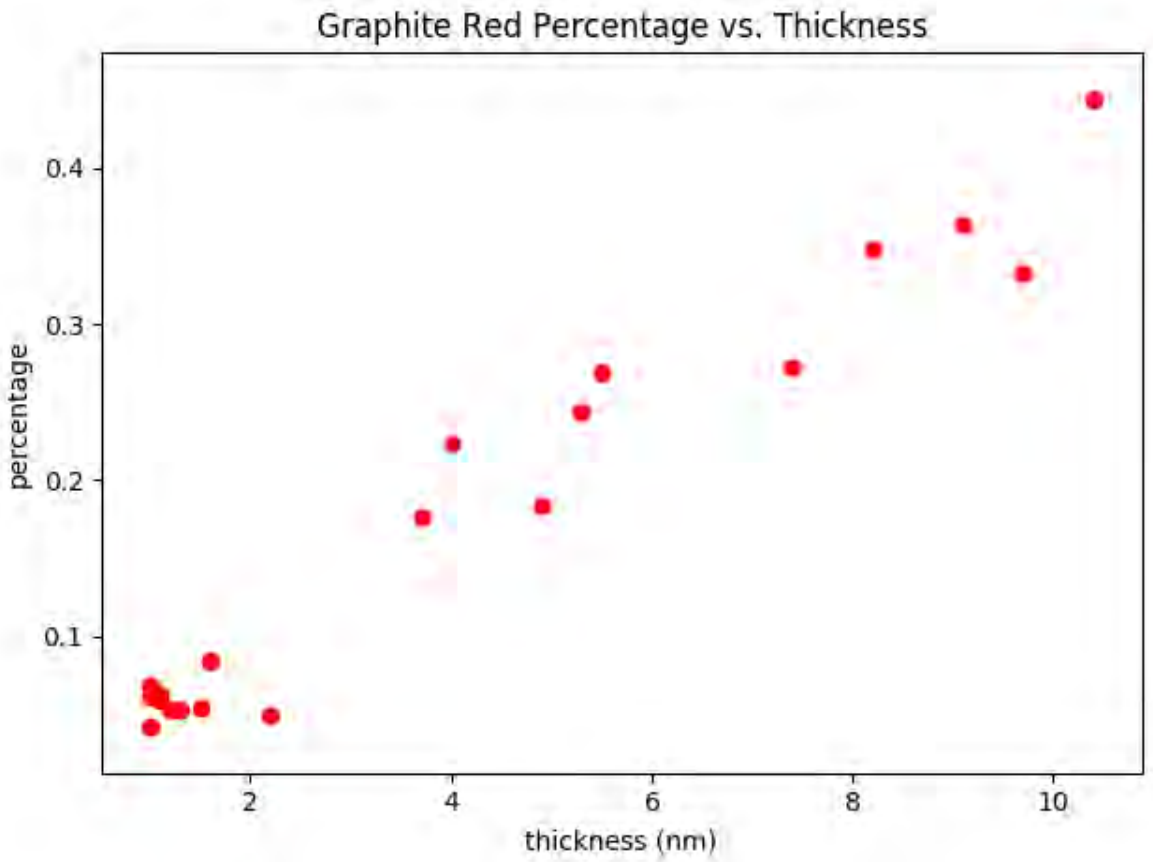

Figure 2.3: Plot of red % difference against AFM thickness of graphite. The % difference was calculated by the equation: % diff = (background - flake) / background.

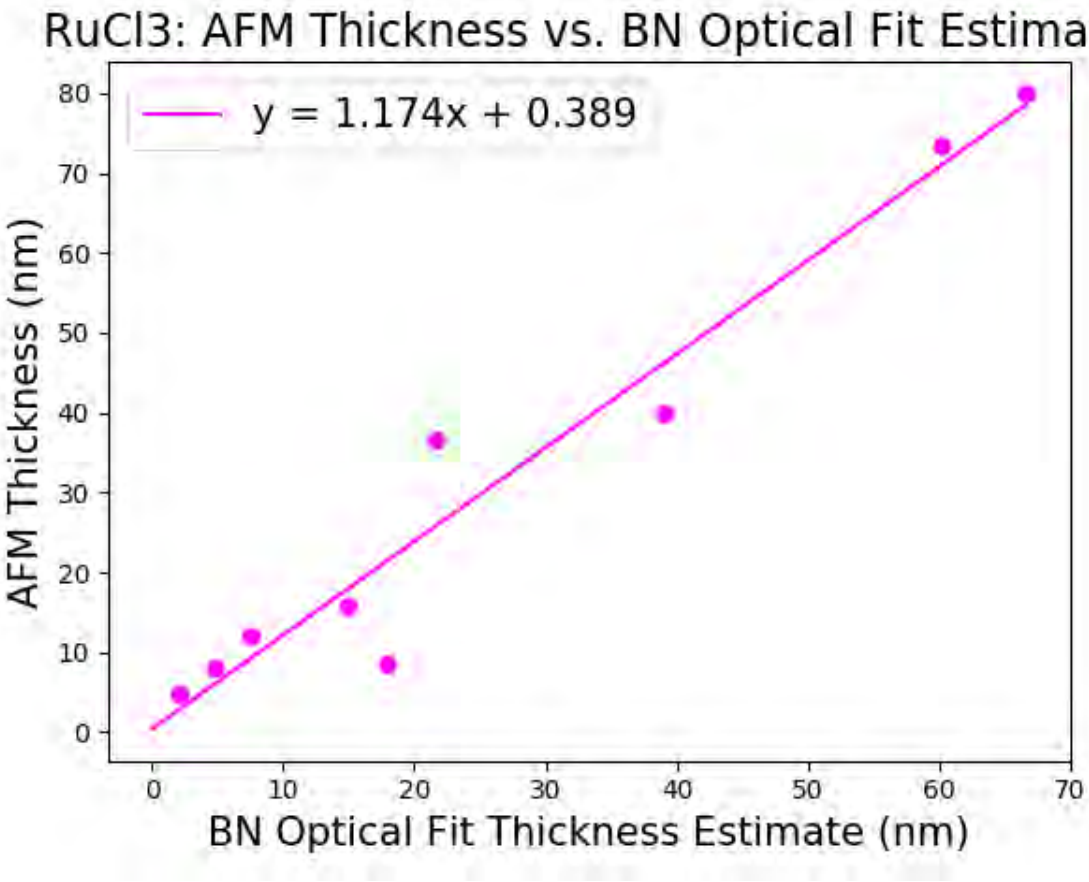

Figure 2.4: Plot of the AFM thickness measurements of $RuCl_3$ flakes against the thickness estimation from the green linear plot of BN thicknesses.

the BN flake showed a slope close to 1 when compared to the AFM thicknesses, suggesting that BN optical thickness estimate is a good estimate for $RuCl_3$ as well.

2.3 Raman Spectroscopy of $RuCl_3$

2.3.1 Raman Spectroscopy

A Raman spectroscopy is a spectroscopic technique that observes low frequency modes such as vibrational and rotational modes within a system by shining a monochromatic laser light onto a system of interest. A Raman spectroscopic data can serve as a structural fingerprint of molecules

or crystals. Molecules excited to higher energy levels inelastically scatter photons by absorbing or releasing some energy from or to photons, thus re-emitting photons with lower or higher frequencies. The shifts in frequencies of photons are due to transitions between various rotational and vibrational states of the molecule. While rotational states are difficult to be observed in non-gaseous materials due to their small nature, and thus the majority of Raman spectrum reflect the vibrational transitions of molecules. The intensity of Raman response is proportional to the changes in the electric dipole-electric dipole polarizability induced by changes in the vibrational and rotational states, and thus only materials with electric dipole-electric dipole polarizability can produce a Raman response. Bonds best suited to be characterized via Raman are relatively neutral bonds (as opposed to polar bonds such as C-O or O-H) because under vibrational motion, neutral bonds undergo large changes in polarizability whereas polar bonds undergo large changes in the net dipole moment.

2.3.2 Spectroscopic Data

Raman spectroscopy was taken of $RuCl_3$ flakes of thicknesses ranging from 1.5 nm to 76 nm. The excitation wavelength was at 532 nm, with a blaze grating of 600 g/mm across 500 nm. The center wavelength was 595.275 nm, with a spectral center of 1997.525 1/cm. The laser spot size was approximately 1 μn in radius and approximately 1 μm in depth. The Raman data was taken with an integration time of 0.52346 s with 100 accumulations per data set. The thicknesses of the $RuCl_3$ flakes were estimated by taking an average of the thickness estimates provided by sine fits of BN blue and red optical data when the optical data of the $RuCl_3$ was inputted. The BN thickness estimate was used to estimate the thickness of the $RuCl_3$ flakes because $RuCl_3$ and BN are both insulators and are expected to have similar optical response with regards to flake thickness.

While taking the Raman spectroscopy data, the laser was focused on the SiO_2 surface, and the response of the SiO_2 peak was controlled to be around 500 counts in oscilloscope mode. For each Raman data of a flake, a Raman data of the SiO_2 in the vicinity of the flake was also taken to

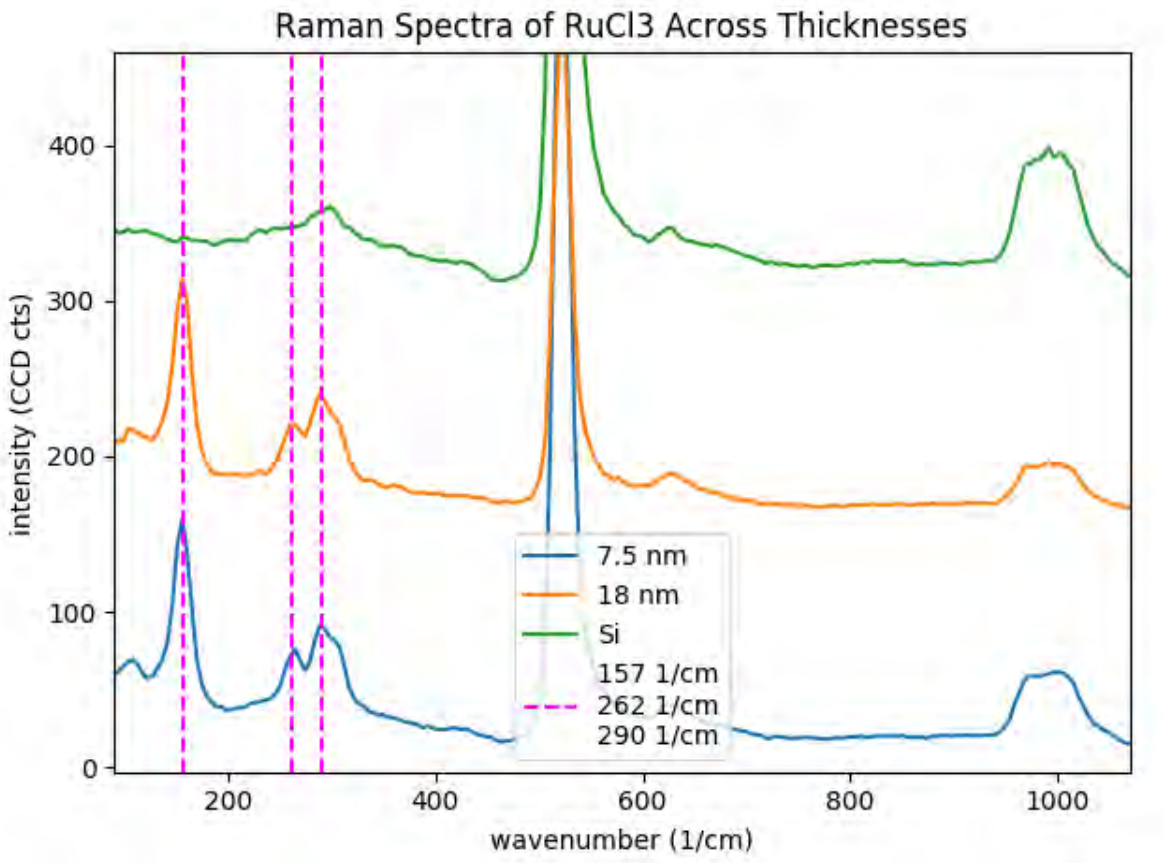

Figure 2.5: The peaks at 155 1/cm, 262 1/cm, and 290 1/cm are $RuCl_3$ peaks. The SiO_2 peak is at 500 1/cm, with a resonance peak at 1000 1/cm. No discernible changes are apparent across thicknesses.

ensure consistency of the Raman data across all flakes to provide relative baselines for each flake data.

When the Raman spectra of $RuCl_3$ was plotted at different thicknesses, no shift in the location, height, or width of the $RuCl_3$ peaks were found (see Figure 2.5), thus indicating that little to no thickness dependence exists in the Raman spectra. Similarly, when a bilayer $RuCl_3$ was plotted at day 0 of exfoliation and day 5 of exfoliation, no changes in the location, height, or width of the $RuCl_3$ peaks were found, as shown in Figure 2.6.

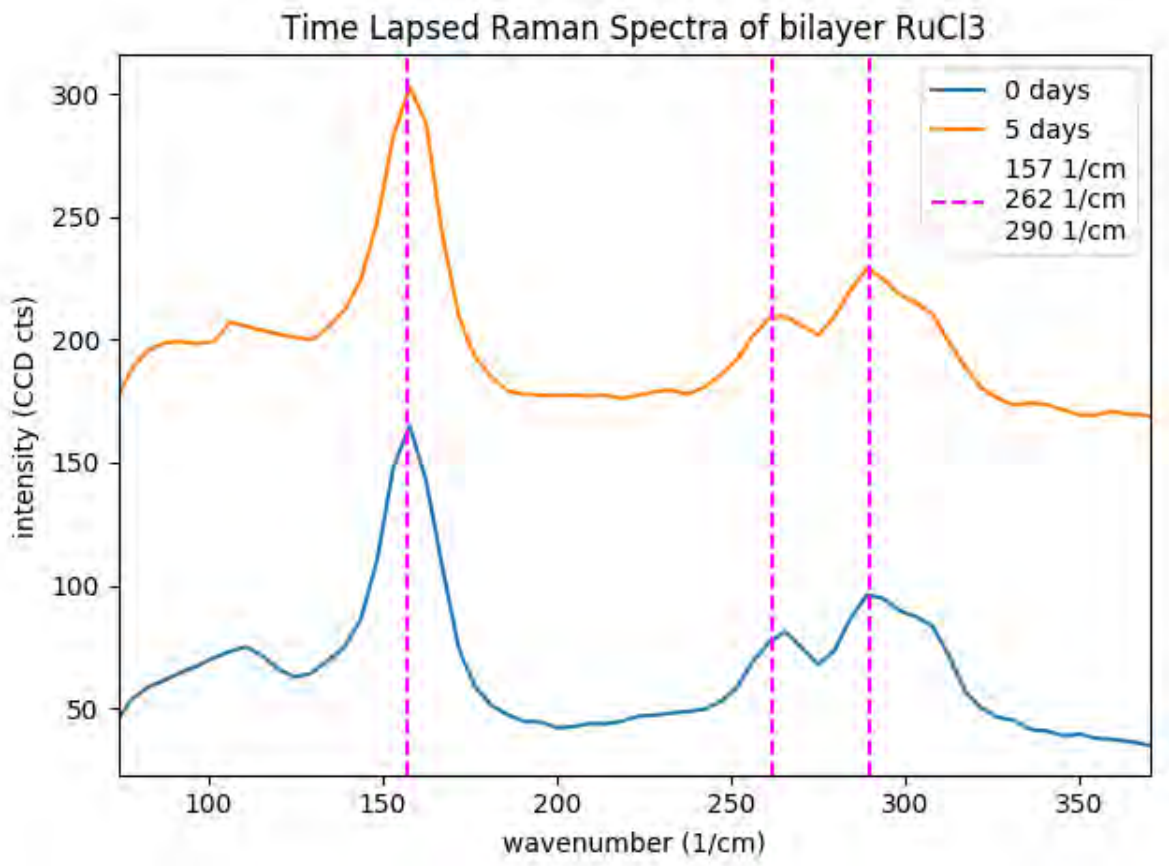

Figure 2.6: Time lapse plot of bilayer $RuCl_3$ from day 0 and day 5. No discernible changes are apparent in the time lapse.

Chapter 3

Heterostructure Assembly and Device Design

3.1 Mechanical Assembly of van der Waals Heterostructures

The van der Waals (vdW) assembly technique allows any 2D material exfoliated from a bulk crystal, with a wide range of physical properties, to be re-assemble into a designer structure [DYM+10, WMH+13]. Stacking two layers of different 2D material creates a unique interface, where the interplay between electron correlation, proximity effect and lattice mismatch combined to give rise to novel emergent quantum phenomena.

Typically, the so-called dry transfer technique utilize a transfer slide as shown in Fig. 3.1 [WMH+13]. Based on the sequential order, a transfer slide is assemble by mounting a polydimethylsiloxane (PDMS) block on a glass slide, pressing a transparent Scotch tape around the PDMS block and attaching a polypropylene carbonate (PPC) film to the transparent tape. The PPC film functions as the sticky layer that picks up the top-most layer of 2D material heterostructure.

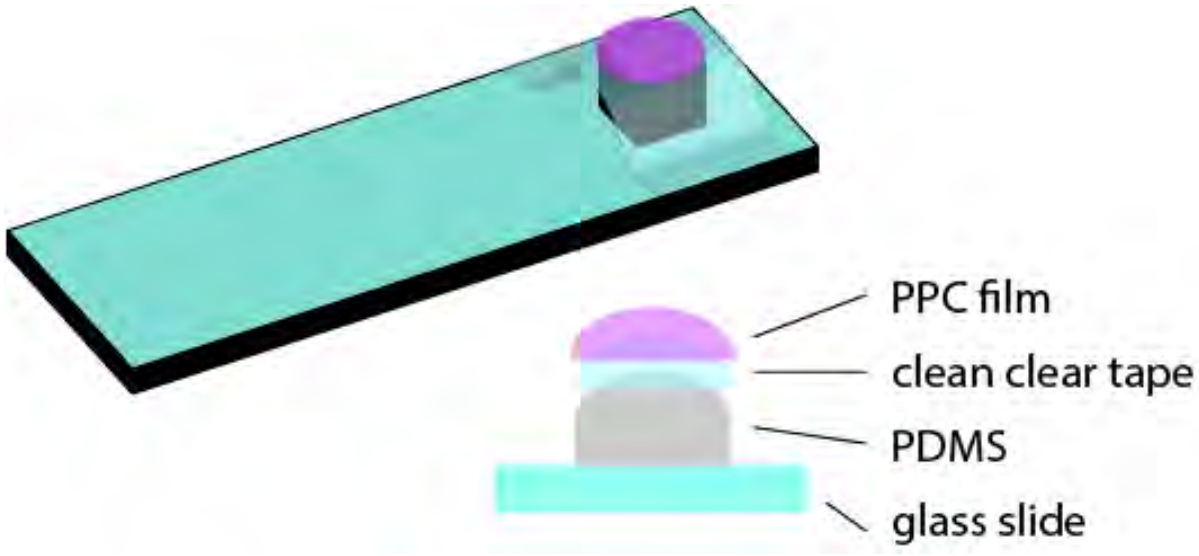

Figure 3.1: Schematic of the glass slide that is ready to start picking up a stack. While the PDMS attached to glass slide via clean clear tape can be prepared far in advance of picking up the stack, layering the PPC film over the PDMS surface is advised to be done within a short period of picking up the stack to prevent contamination of the PPC surface. Notice that the PDMS has a curved surface top. This curved surface is created by pressing down on the clear tape close to the PDMS. Surfaces with an even curvature are best for picking up stacks.

The heterostructures relevant in this thesis all utilize the dual graphite and hBN geometry, to achieve optimal quality [ZSZ+17, LTC+17]. The active part of the heterostructure involves a bilayer graphene (BLG) next to a thin layer of TMDC that is around $\sim$ 10 nm thick. Two graphite layers serve as top and bottom gate electrode, whereas hBN layers are the dielectric medium. For simplicity, we will refer to the two graphite (hBN) layer as top and bottom graphite (hBN), based on its relative positive in final heterostructure. Since PPC does not stick to graphite, a large uniform piece of hexagonal boronitride (hBN) with a thickness of 20 $\sim$ 30 nm is used as the first layer to be picked up. The rest of heterostructure will be picked by the first hBN through vdW interaction. Owing to this unique order, vdW assembly process is also referred to as the top-to-bottom assembly.

An important detail for a successful vdW assembly is a well-defined curvature to the PDMS block, which is created by following several steps. We first take a uniform PDMS that is $\sim$ 1 mm thick and cut out a 2 mm by 2 mm square using a razor blade. When cutting the PDMS, one must

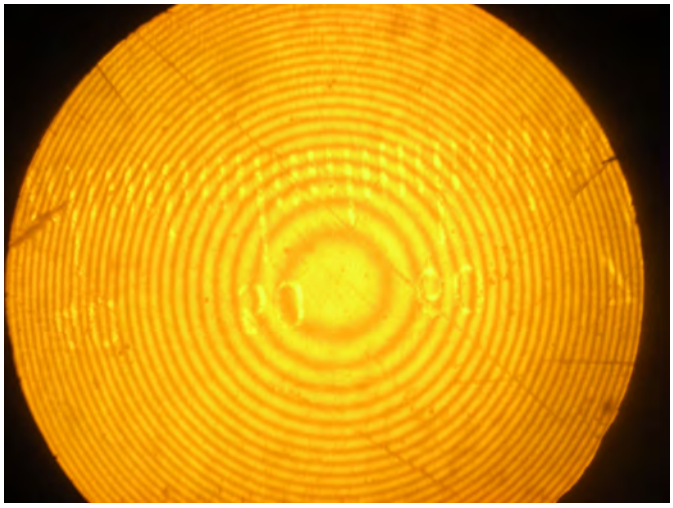

Figure 3.2: An image of Newton rings emanating from the touchdown point in the center. In a PDMS with an even curvature, the Newton rings will emanate out from the center in circular rings. Any deformations in the PDMS will be reflected in the wavefront of the Newton rings, as the rings would no longer be concentric circles and instead would assume various uneven wavefronts. Image source: Wikimedia.

take care to ensure that the edges are straight and vertical. Deformed PDMS can result in uneven curvature of PPC, which would add to the difficulty of the stacking process. A transparent Scotch tape is pressed down around the PDMS using the blunt edge of two razor blades. This introduce a uniform curvature on the PDMS. Next, a PPC film is prepared by spin coating a clean Si chip with PPC at 3450 rpm for 1 minute. A razor blade is then used to scrape off a tiny portion of PPC from a corner of the chip. A circular hole is punched into the middle of a clear tape (not necessarily clean) using a hole punch, and the tape is placed over the Si chip with PPC, ensuring that the hole is completely inside the chip surface. The tape is pulled back slowly starting from the corner at which the PPC has been scratched off. A PPC film should cover the hole. This PPC film is then placed over the curved surface of PDMS, and the surrounding tape is pushed onto the glass slide. After removing the excess tape from the glass slide, the PPC is ready to pick up a stack. The schematic of prepared glass is shown in Figure 3.1. While the glass slides with taped PDMS can be stored for a long time, the PPC film is advised to be used soon after being made, because extraneous materials may stick to PPC due to its sticky nature and dirty the glass slide, perhaps even rendering it unusable.

The procedure of picking up a 2D material flake is described as the following. By mounting the transfer slide on the micro-manipulator of the transfer station, the operating surface of PPC film face downward, so that it could be lowered near the surface of a SiO_2/Si substrate. The initial point of contact between the transfer slide (and PPC) to the substrate is referred to as the touch-down point, which should be aligned very close to the flake of interest, usually at one corner of the flake. The touch down point can be observed via the formation of Newton rings, which are concentric circles of waves emanating from the point of contact (see Figure 3.2 for reference). To pick up the top-top BN, two methods can be attempted–a quick retraction method vs. a slow retraction method. During the quick retraction method, the glass slide is pressed down just enough to cover the entirety of the flake of interest with PPC, and then is quickly retracted from the chip such that the PPC jumps. This method can result in the BN flake ripping, particularly if the flake is very large. For large flakes or for flakes that cannot be picked up using the quick retraction method, the slow retraction method can be used to pick up the flakes. In the slow retraction method, the flake is covered with PPC, and then the glass slide is very slowly retracted such that the Newton ring moves slowly and evenly across the flake. Every time a flake is picked up and the glass slide is fully retracted from the chip, the glass slide is baked at 90°C for 1 minute to reduce deformation of PPC.

Before picking up subsequent layers, the stack on the glass slide is imaged, and the flake of interest is carefully aligned with the stack on the glass slide to create the optimal heterostructure. From the second layer and beyond, all flakes must be picked up using the slow retraction method because the stack may get damaged when PPC jumps. It is important to note that layers cannot be picked up in certain order. For example, BN and graphite can pick each other up, but PPC cannot pick up graphite. Similarly, $RuCl_3$ can pick up graphite and vice versa, but PPC cannot pick up $RuCl_3$. During the heterostructure construction process, BN was found to be unable to pick up $RuCl_3$. Once the entire stack has be picked up on the glass slide, the stack needs to be mounted on the destination chip. Also, the graphite being picked up must be smaller than the BN that is picking up the flake because otherwise, the vdW pull on BN from graphite can remove BN from the PPC.

Once BN has been left behind on top of the graphite, there is no way to pick up the stack again onto PPC.

Bubbles affect the quality of the data taken using the device because the spin orbit coupling proximity effect decreases exponentially with increasing interlayer distance [**?**], so if possible, getting rid of the bubbles during the mounting step can increase the quality of the device. To mount the stack, a desired destination chip, usually one with line markers, is placed in the mechanical transfer station set at a temperature of 40°C. After properly aligning the glass slide with the line markers, the glass slide is lowered to the chip until Newton rings are visible and the temperature is increased 1°C at a time while properly adjusting the height of the glass slide such that the Newton rings do not move too far from the flake.

Now, to remove bubbles, the PPC must touch down only on one side of the stack while increasing the temperature 1°C at a time. At around 73°C, the PPC film assume a straight wavefront with narrow Newton rings. Ensuring that the PPC is touching down on the chip only on one side of the stack, the wavefront is slowly swept across the stack over ∼10 minutes back and forth by manually lifting up and pressing down the glass slide over the line marker chip. The bubbles are swept to the side along the wavefront, either being released outside of the stack, or combining with nearby bubbles to form a larger bubble. The temperature is constantly increased during this sweeping process, with the wavefront moving only as a result of height change in the glass slide. The bubbles were successfully pushed alongside the wavefront in a stack with WSe_2, but this method should be avoided when mounting stacks with brittle materials such as $RuCl_3$, which may crack during the process. The PPC may touch down on both sides of the stack if no attempt will be made to remove the bubbles.

The temperature is increased until 120°C. The PPC will start melting at ∼90°C, and by 120°C, the PPC will assume finger-like shapes as shown in Figure 3.3. At this point, the glass slide is slowly retracted mechanically from the chip while taking care to make sure that the PPC does not jump, as the structure may become misaligned or wrinkled when the PPC jumps. Once the glass

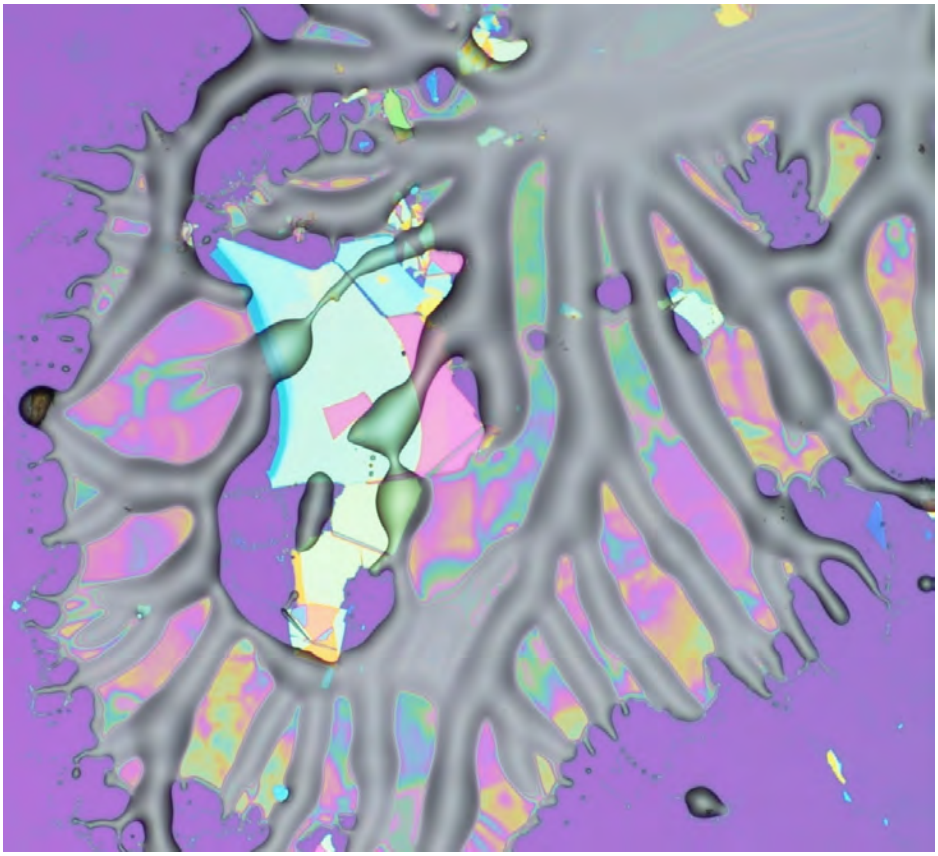

Figure 3.3: This is an image of the finger-like structure of molten PPC on a chip with desired stack. PPC begins to melt at around 90°C, but due to the high viscosity of molten PPC, PPC start to show finger-like edges. As the glass slide is slowly retracted from the chip, the molten PPC behind a trail such as in this image. This residual PPC is later cleaned off the chip via either annealing or acetone wash.

slide is fully retracted (leaving behind molten PPC residue), the chip is rapidly cooled to 40°C.

The PPC residue can be removed either through annealing or through acetone wash. While annealing can more effectively remove PPC, annealing should not be used when working with structures containing transition metal complexes because transition metal complexes are not very stable and may degrade under high heat. In the annealing method, the structure is placed into an oven and is subjected to a temperature of 400°C for 1 hour before cooling down to room temperature naturally. In the acetone wash method, the structure is subjected to a continuous stream of acetone for 30 seconds, before being subjected to a continuous stream of isopropanol for 30 seconds. The acetone is not allowed to dry before being washed away with isopropanol.

Afterwards, the stack is dried with nitrogen gas.

In this thesis, two types of heterostructures were constructed: 1) BN-Graphite-BN-WSe_2-bilayer Graphene-BN-Graphite with a control device of BN-Graphite-BN-bilayer Graphene-BN-Graphite (see Figure 3.4) and 2) BN-Graphite-$RuCl_3$-bilayer Graphene-BN-Graphite with a control device of BN-Graphite-BN-bilayer Graphene-BN-Graphite (see Figure 3.8).

3.2 WSe_2-bilayer Graphene

WSe_2 is a semiconducting group-VI transition metal dichalcogenide (TMDC) composed of tungsten and selenium ligands covalently bound to form a hexagonal crystalline structure such that each tungsten atom is bound to six selenium ligands in a trigonal prismatic coordination geometry and each selenium ligand is bound to three tungsten atoms in a trigonal prismatic coordination geometry. WSe_2 is a semiconductor and could be doped with p-type charge carriers (holes) by electrostatic gating. It is chemically inert, and has a flat two-dimensional structure. When graphene is placed in contact with a TMDC, a weak hybridization occurs at the boundary to increase the strength of SOC in graphene [**?**]. It has been proposed that with sufficiently strong SOC, graphene could support a ground state similar to a topological insulator [KM05b, **?**].

The WSe_2-Graphene heterostructure has been previously explored as a method of introducing SOC in graphene. These heterostructures are probed with magnetoresistance measurement, and a weak anti-localization peak, as shown in Fig. 3.6b is used as indication for induced SOC. The interpretation of magnetoresistance measurement is complicated by the high level of device disorder, which has a large influence on magnetoresistance measurement. To better characterize proximity induced SOC, a better-defined method and higher quality sample are required.

We propose to characterize induced SOC using the high field phase diagram of bilayer graphene, as shown in Fig. 3.7 [LTC$^+$17]. Horizontal black lines in the phase diagram mark displacement field induced phase transition between ground states with different layer, orbital and spin quantum

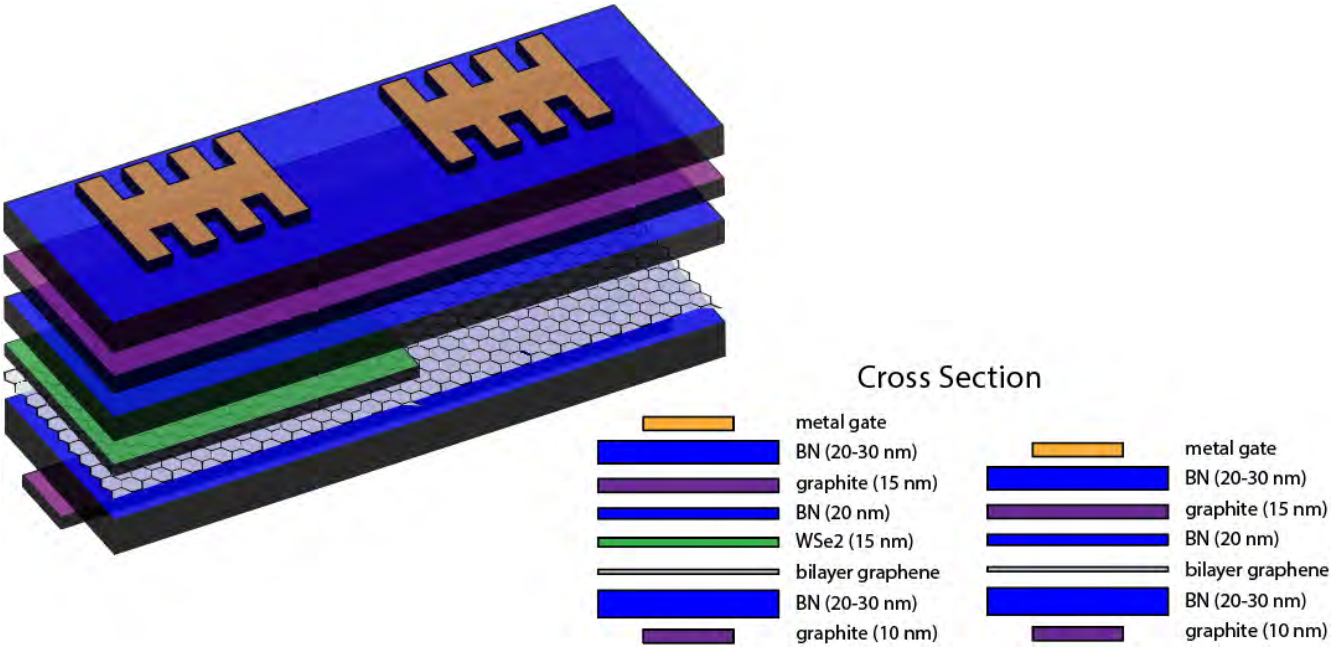

Figure 3.4: Schematic for the WSe_2-Graphene device.

number, in the absence of SOC. By placing BLG next to a WSe_2 crystal, proximity effect would induce SOC in the adjacent graphene layer, shifting the boundary of phase transitions. By fabricating a device where a portion of BLG is in contact with WSe_2 while the other half encapsulated with hBN and graphite, the difference in phase boundary will provide a clear characterization of proximity induced SOC effect.

3.3 $RuCl_3$-bilayer graphene

The second structure that was constructed was a 7-layer structure of BN-graphite-$RuCl_3$-bilayer graphene-BN-graphite with a control device of BN-graphite-BN-bilayer-graphene-BN-graphite. A control device made of BN-graphene interface was constructed because BN-graphene device has been extensively studied, and could provide control for structure quality and test setup when studying proximal effect of $RuCl_3$ on graphene.

In this structure $RuCl_3$ was place on top of graphene for two experimental purposes: 1) to observe

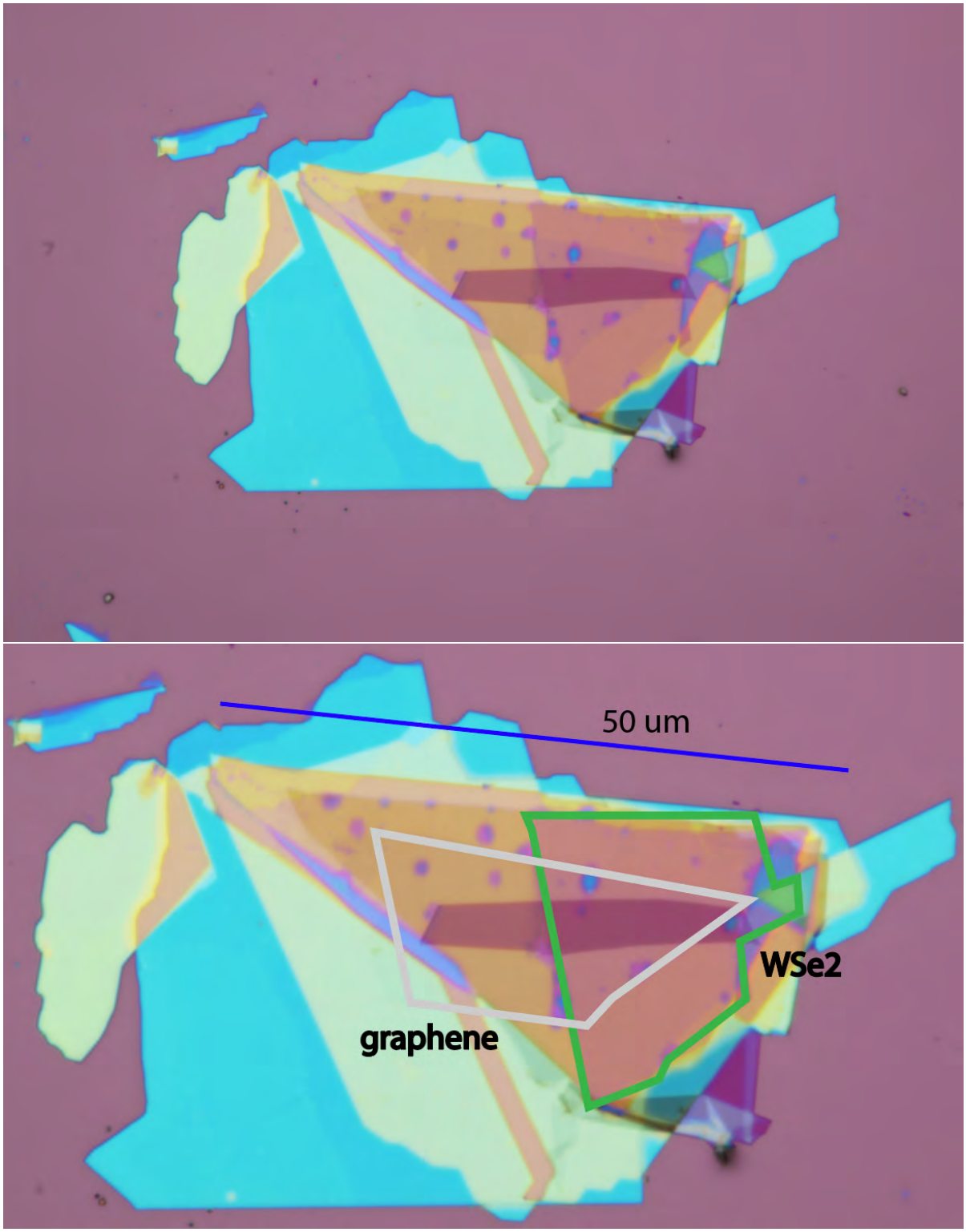

Figure 3.5: A device of BN-Graphite-BN-WSe_2-Graphene(bilayer)-BN-Graphite-SiO_2. Top: Regular optical picture. Bottom: Zoom in of the structure with graphene and WSe_2 labelled.

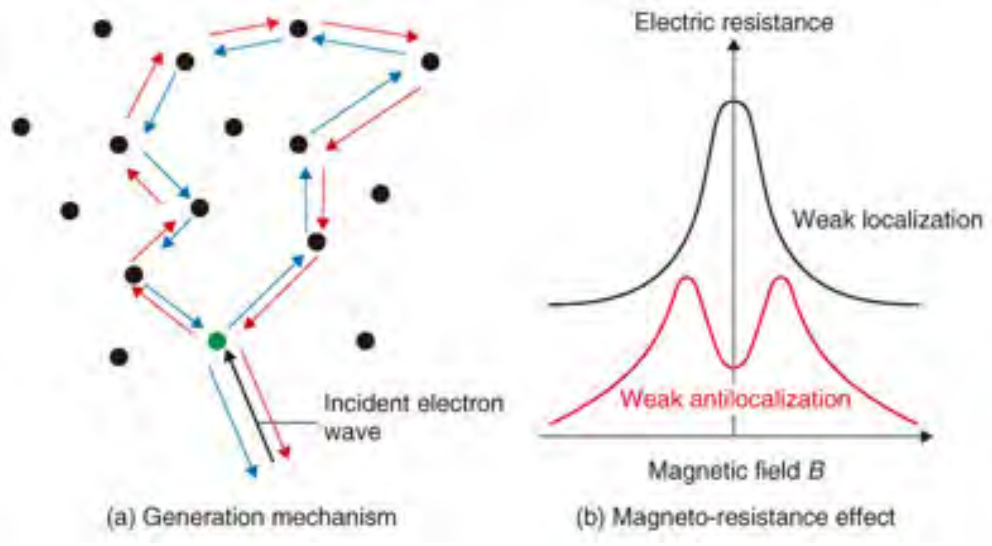

Figure 3.6: Left: Different paths that can be taken by incident electron wave. Right: Magnetoresistance curves obtained for weak localization (no SOC) and weak anti-localization (SOC).

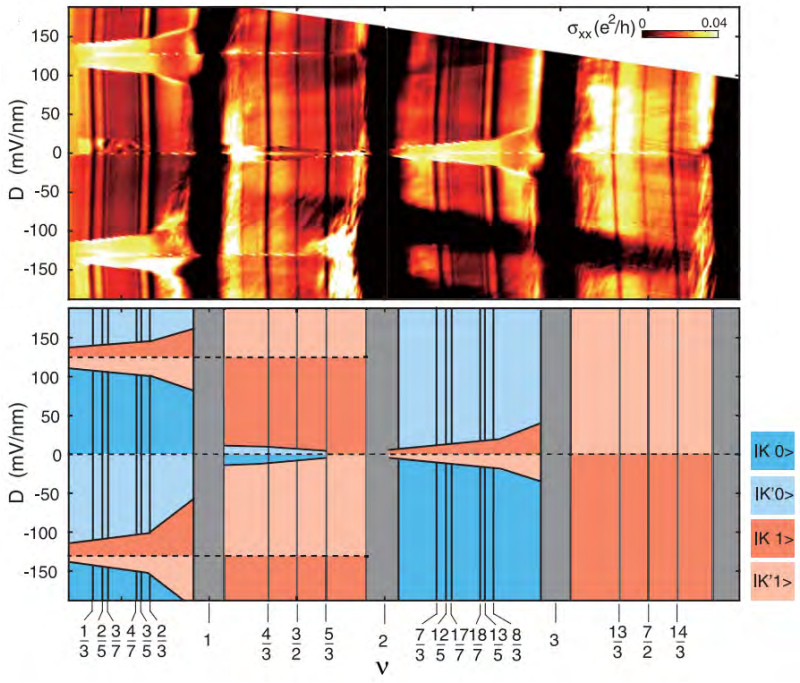

Figure 3.7: (a) Longitudinal conductance σ_{xx} of BLG at $T = 0.2$ K and $B = 14.7$ T versus filling factor ν and displacement field D for the LLL of bilayer graphene, $0 \leq \nu \leq 4$. (b) Schematic phase diagram labeling the ground sate order for the same filling fraction range as shown in (a). The blue (red) shaded area is occupied by broken-symmetry states with orbital index 0 (1), whereas the dark and light color tones denote the two different valley-isospin (layer) polarizations. Dashed and solid black lines correspond to phase transitions between broken-symmetry states with different valley-isospin and orbital index, respectively. Vertical solid lines represent incompressible states observed in transport measurements.

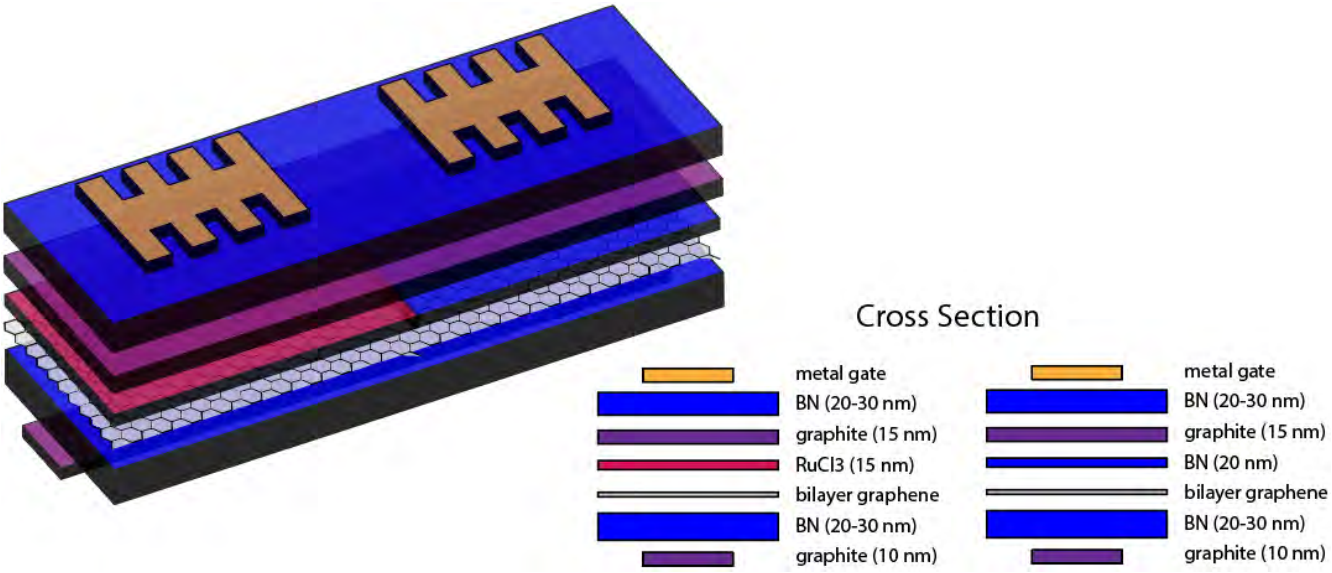

Figure 3.8: Schematic for the $RuCl_3$-Graphene device.

spin order phase transition in $RuCl_3$ via proximity effect in graphene, and 2) to observe thermal Hall effect modulated by Majorana fermions in $RuCl_3$.

At low temperatures, $RuCl_3$ was measured to exhibit a zigzag antiferromagnetic (AFM) order at low in-plane magnetic field, and a non-topological long-range magnetic order at high in-plane magnetic field. The expectation today is that between the zigzag AFM phase and the non-topological phase lies a QSL phase with half-integer quantization. The first principles calculations by Yang *et al.* in 2013 showed that graphene is highly sensitive to the magnetic ordering of nearby magnetic insulators. The bilayer graphene in contact with $RuCl_3$ then serves as an indirect measurement of the magnetic spin (dis)order in the $RuCl_3$ as well as the strength of the proximity effect of $RuCl_3$ on graphene. Furthermore, graphene is highly stable under strong magnetic fields, thus allowing measurements of spin order in $RuCl_3$ across a wide range of magnetic field strength needed to characterize the QSL phase.

Secondly, one of the main reasons that $RuCl_3$ began to be suspected as a Kitaev QSL is the thermal conductance observed in $RuCl_3$ at very low temperatures as mentioned previously. $RuCl_3$ is a very strong insulator, and thus exhibit little to no mobile charge carriers, and observation of quantized thermal Hall conductance could potentially suggest existence of Majorana fermions modulating

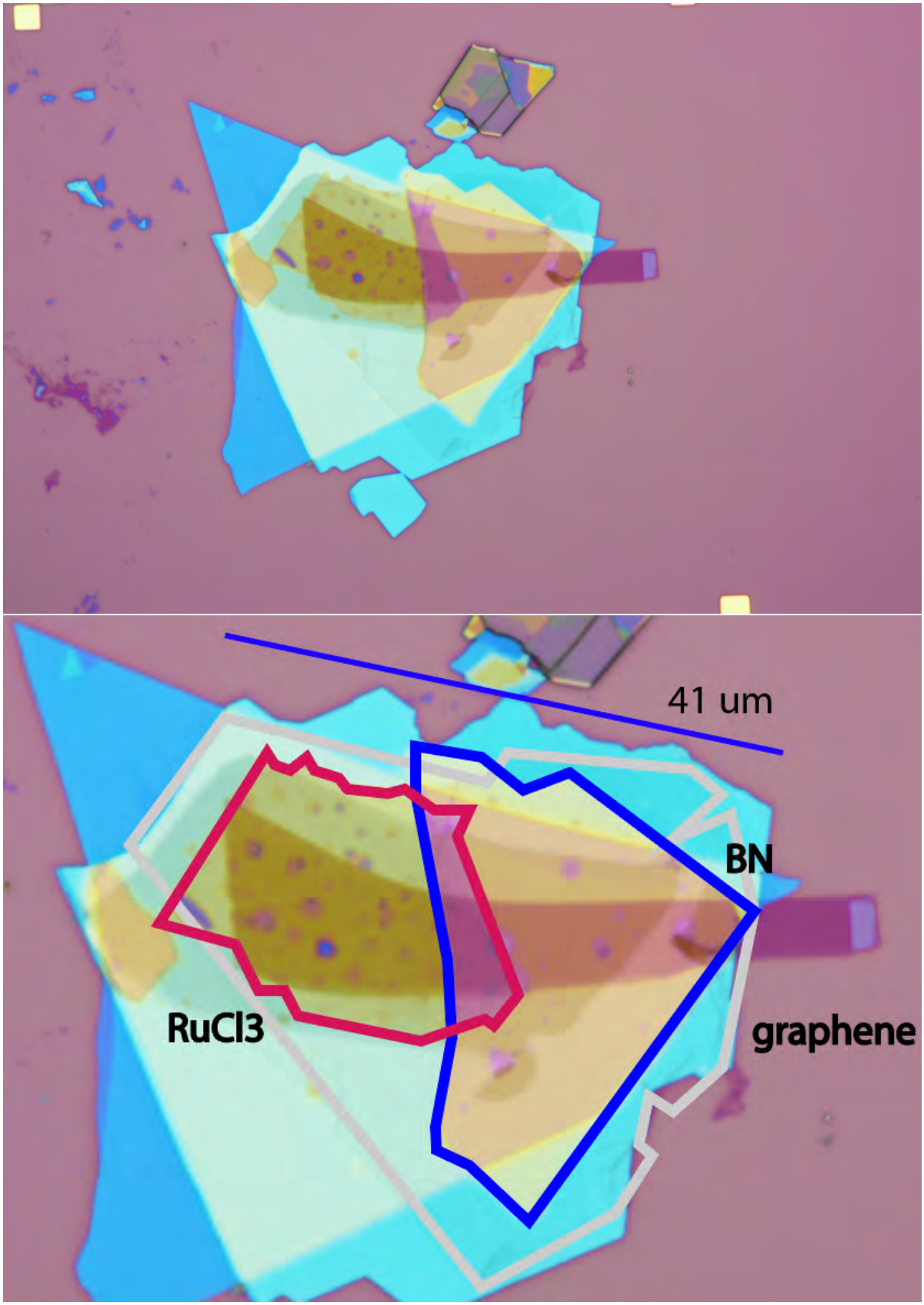

Figure 3.9: A device of BN-Graphite-$RuCl_3$+BN-Graphene(bilayer)-BN-Graphite-SiO_2. Top: Regular optical picture. Bottom: Zoom in of the structure with graphene, $RuCl_3$, and WSe_2 labelled.

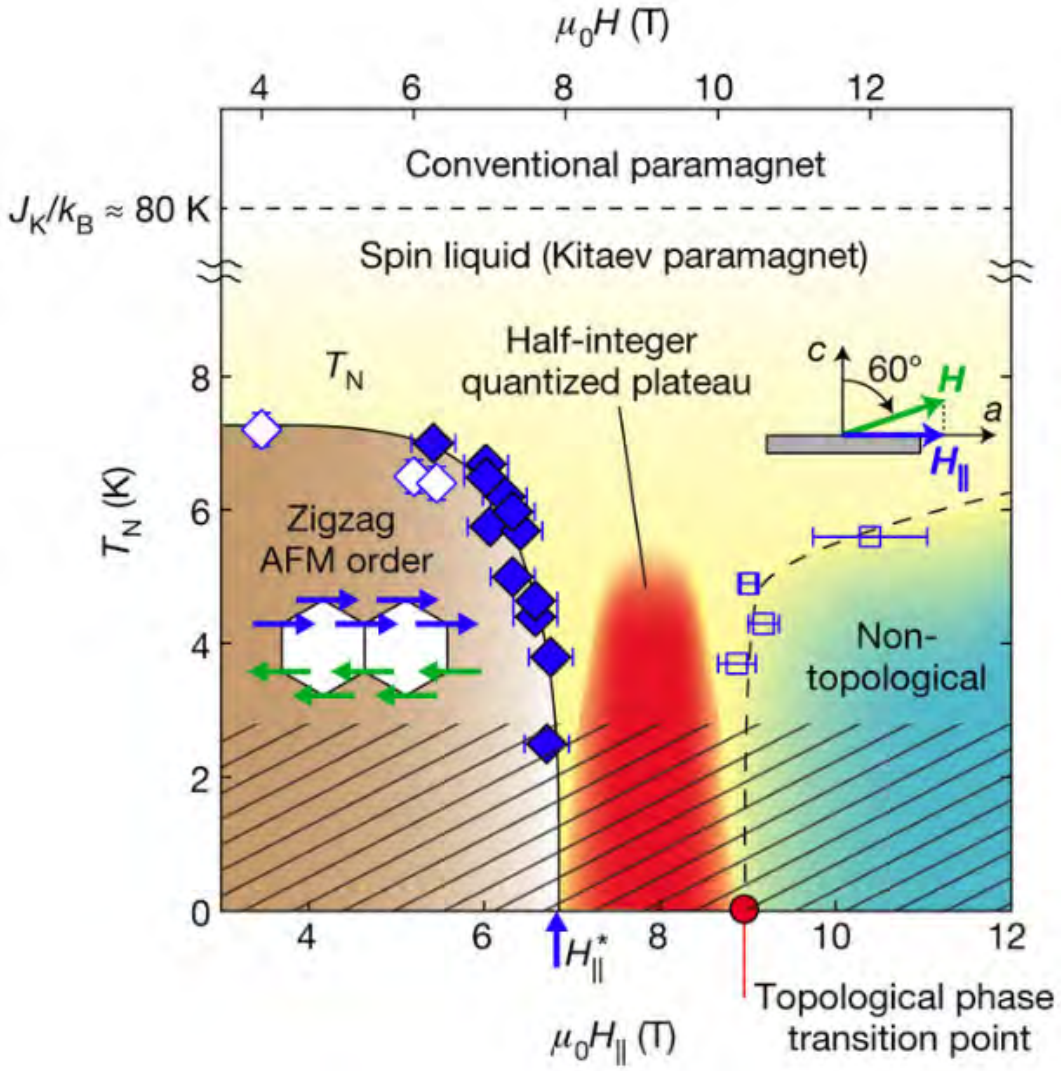

Figure 3.10: Phases of magnetic spin order in $RuCl_3$ across different external magnetic field strength. $RuCl_3$ starts with zigzag AFM magnetic order at low magnetic field and at low temperature, and have shown to have a long range magnetic order at high magnetic field and low temperatures. Current expectation is that a quantum spin liquid phase lies between the zigzag AFM phase and the non-topological phase. Image Source: [KOM+18b]

the heat transport. However, getting a thermometer to thermalize in contact with an insulator to measure conductance is challenging. To resolve this problem, the graphene in contact with $RuCl_3$ can be used as the thermometer. This graphene interface is very important because thermometer needs to have a low heat capacity (i.e. responds well to heat change) and graphene couples well to $RuCl_3$ via 2D interface.

3.4 Design

DesignCAD software was used to construct the design of the device. Multiple pictures of the stack was taken using the align marker, and the images were loaded into the DesignCAD software. Afterwards, a Hall bar with 6 or 8 contact points were constructed in the area of the device containing every layer, with the contact point reaching outside of the bottom graphite gate to reach area with only BN-graphite-BN/WSe_2/$RuCl_3$-graphene-BN. Leads were designed to connect the contact point of the Hall bar to the larger chip contacts, and two more contacts were made from the bottom graphite to larger chip contacts, all while ensuring that there is no shorting such as graphene-graphite contact, or lead-lead contact. After designing the Hall bar, the area at which the device will be etched was designed. Three types of etches were designed on the device–a graphene etch and a graphite etch. In a graphene etch, the stack is etched away until the graphene is etched, the graphite etch etches away until the bottom graphite is exposed (i.e. etched until the bottom BN is etched away). The device designs for the $RuCl_3$ and WSe_2 devices are shown in Figure 3.11.

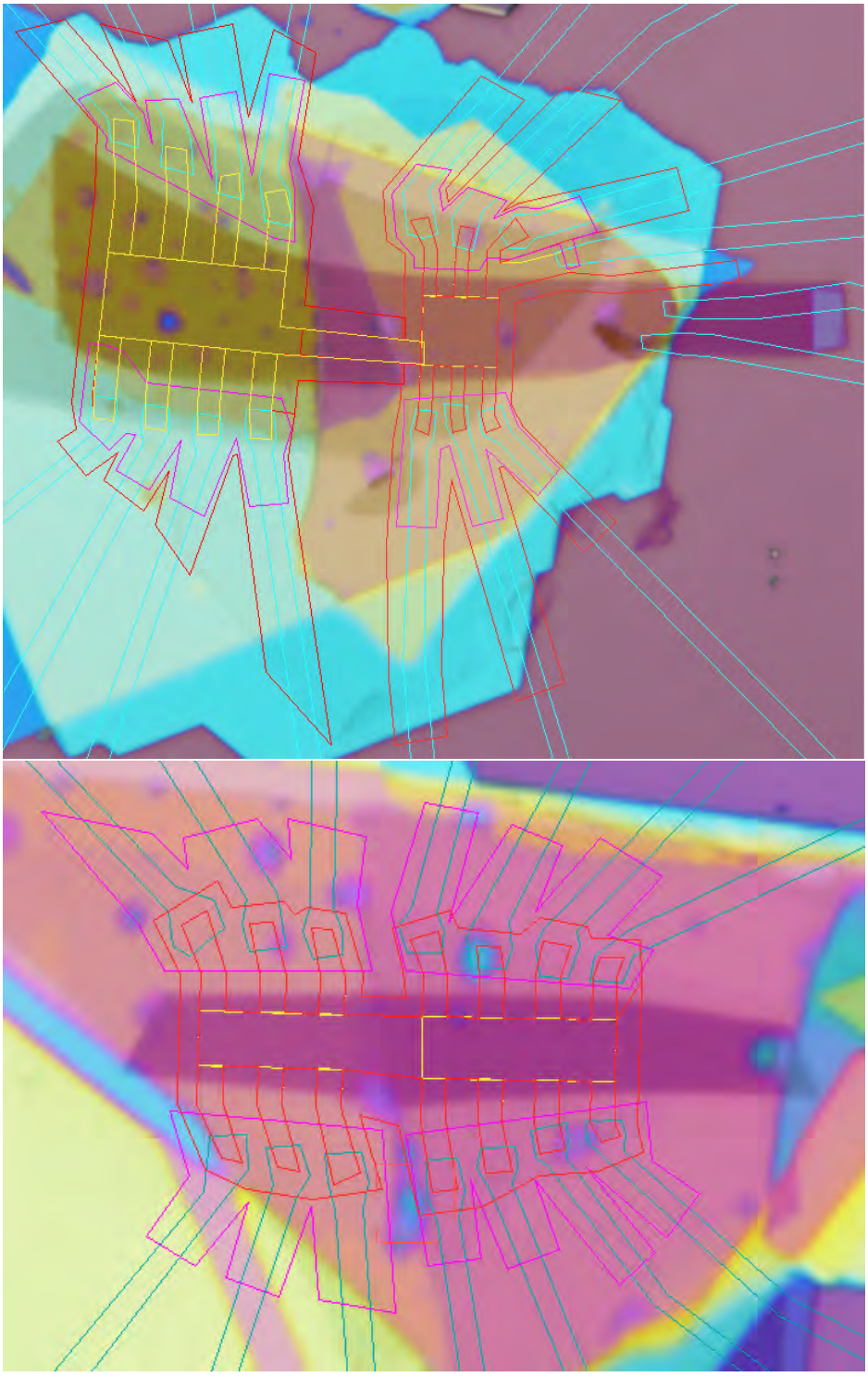

Figure 3.11: DesignCAD Hall bar designs for $RuCl_3$-graphene device (top) and WSe_2-graphene device (bottom). The yellow outlines show the location of the gold metal gate, the pink show the outlines of the graphene etch, and the red shows the outlines of graphite etch. The nanofabrications will be conducted in the upcoming month.

Chapter 4

Conclusion

4.1 Summary of Thesis Achievements

In this thesis, I achieved

1. optical thickness estimates of graphite and BN,
2. Raman spectroscopy of $RuCl_3$ flakes of thicknesses ranging from 1.5 nm to 76 nm,
3. a construction of a BN-graphite-BN-WSe_2-bilayer graphene-BN-graphite device with a control device of BN-graphite-BN-bilayer graphene-BN-graphite, and designed the Hall bar device and relevant etch masks on DesignCAD, and
4. a construction of a BN-graphite-$RuCl_3$-bilayer graphene-BN-graphite with a control device of BN-graphite-BN-bilayer graphene-BN-graphite, and designed the Hall bar device and relevant etch masks on DesignCAD.

Bibliography

[AM76] Neil W. Ashcroft and N. David Mermin. *Solid State Physics*. Cengage Learning, 1976.

[AMU75] Tsuneya Ando, Yukio Matsumoto, and Yasutada Uemura. Theory of hall effect in a two-dimensional electron system. *Journal of the Physical Society of Japan*, 39(2):279–288, 1975.

[And73] P. W. Anderson. Resonating valence bonds: A new kind of insulator? *Mat. Res. Bul.*, 8:153–160, Feb 1973.

[Blu01] Stephen Blundell. *Magnetism in Condensed Matter*. Oxford University Press, 2001.

[CZF+13] Cui-Zu Chang, Jinsong Zhang, Xiao Feng, Jie Shen, Zuocheng Zhang, Minghua Guo, Kang Li, Yunbo Ou, Pang Wei, Li-Li Wang, Zhong-Qing Ji, Yang Feng, Shuaihua Ji, Xi Chen, Jinfeng Jia, Xi Dai, Zhong Fang, Shou-Cheng Zhang, Ke He, Yayu Wang, Li Lu, Xu-Cun Ma, and Qi-Kun Xue. Experimental observation of the quantum anomalous hall effect in a magnetic topological insulator. *Science*, 340(6129):167–170, 2013.

[DP71a] Mikhail I. Dyakonov and Vladimir I. Perel. Current-induced spin orientation of electrons in semiconductors. *Phys. Lett. A*, 35:459–460, Jul 1971.

[DP71b] Mikhail I. Dyakonov and Vladimir I. Perel. Possibility of orienting electron spins with current. *Sov. Phys. JETP Lett.*, 13:657–660, Jun 1971.

[DPY+17] Seung-Hwan Do, Sang-Youn Park, Junki Yoshitake, Joji Nasu, Yukitoshi Motome, Yong-Seung Kwon, D. T. Adroja, D.J. Voneshen, Kyoo Kim, T.-H. Jang, J.-H. Park, Kwang-Yong Choi, and Sungdae Ji. Majorana fermions in the kitaev quantum spin system α-rucl$_3$. *Nat. Phys. Let.*, 13:1079–1085, Sep 2017.

[DYM+10] C. R. Dean, A. F. Young, I. Meric, C. Lee, L. Wang, S. Sorgenfrei, K. Watanabe, T. Taniguchi, P. Kim, K. L. Shepard, and J Hone. Boron nitride substrates for high-quality graphene electronics. *Nature Nanotechnology*, 5:722–726, Aug 2010.

[Hal79] E. H. Hall. On a new action of the magnet on electric currents. *American Journal of Mathematics*, 2(3):287–292, 1879.

[Hal81] E. H. Hall. On the rotational coefficient in nickel and cobalt. *The London, Edinburgh, and Dublin Philosophical Magazine and Journal of Science*, 12(74):157–172, 1881.

[Hol09] Sharon Ann Holgate. *Understanding Solid State Physics*. CRC Press, 2009.

[HR88] F. D. M. Haldane and E. H. Rezayi. Spin-singlet wave function for the half-integral quantum hall effect. *Phys. Rev. Lett.*, 60:956–959, Mar 1988.

[Kit05] A.Yu. Kitaev. Anyons in an exactly solved model and beyond. *Annals of Physics*, 321:2–111, 06 2005.

[KM05a] C. L. Kane and E. J. Mele. Quantum spin hall effect in graphene. *Phys. Rev. Lett.*, 95:226801, Nov 2005.

[KM05b] C. L. Kane and E. J. Mele. Quantum spin hall effect in graphene. *Phys. Rev. Lett.*, 95:226801, Nov 2005.

[KMGA04] Y. K. Kato, R. C. Myers, A. C. Gossard, and D. D. Awschalom. Observation of the spin hall effect in semiconductors. *Science*, 306(5703):1910–1913, 2004.

[KOM+18a] Y. Kasahara, T. Ohnishi, Y. Mizukami, O. Tanaka, Sixiao Ma, K. Sugii, N. Kurita, H. Tanaka, J. Nasu, Y. Motome, T. Shibauchi, and Y. Matsuda. Majorana quantization and half-integer thermal quantum hall effect in a kitaev spin liquid. *Nature*, 559:227–231, Jul 2018.

[KOM+18b] Y Kasahara, T Ohnishi, Y Mizukami, O Tanaka, Sixiao Ma, K Sugii, N Kurita, H Tanaka, Joji Nasu, Y Motome, T Shibauchi, and Y Matsuda. Majorana quantization and half-integer thermal quantum hall effect in a kitaev spin liquid, 07 2018.

[KWB+07] Markus König, Steffen Wiedmann, Christoph Brüne, Andreas Roth, Hartmut Buhmann, Laurens W. Molenkamp, Xiao-Liang Qi, and Shou-Cheng Zhang. Quantum spin hall insulator state in hgte quantum wells. *Science*, 318(5851):766–770, 2007.

[LTC+17] J. I. A. Li, C. Tan, S. Chen, Y. Zeng, T. Taniguchi, K. Watanabe, J. Hone, and C. R. Dean. Even-denominator fractional quantum hall states in bilayer graphene. *Science*, 358(6363):648–652, 2017.

[MFT14] Gary L. Miessler, Paul J. Fischer, and Donald A. Tarr. *Inorganic Chemistry*. Pearson, 2014.

[NGM+04] K. S. Novoselov, A. K. Geim, S. V. Morozov, D. Jiang, Y. Zhang, S. V. Dubonos, I. V. Grigorieva, and A. A. Firsov. Electric field effect in atomically thin carbon films. *Science*, 306(5696):666–669, 2004.

[SYLY+17] Javier D Sanchez-Yamagishi, Jason Y Luo, Andrea F Young, Benjamin M Hunt, Kenji Watanabe, Takashi Taniguchi, Raymond C Ashoori, and Pablo Jarillo-Herrero. Helical edge states and fractional quantum hall effect in a graphene electron–hole bilayer. *Nature nanotechnology*, 12(2):118, 2017.

[Van18] David Vanderbilt. *Berry Phases in Electronic Structure Theory: Electric Polarization, Orbital Magnetization and Topological Insulators*. Cambridge University Press, 2018.

[vKDP80] Klaus von Klitzing, Gerhard Dorda, and Michael Pepper. New method for high-accuracy determination of the fine-structure constant based on quantized hall resistance. *Phys. Rev. Lett.*, 45:494–497, Aug 1980.

[WMH+13] L Wang, I Meric, PY Huang, Q Gao, Y Gao, H Tran, T Taniguchi, K Watanabe, LM Campos, DA Muller, J Guo, P Kim, J Hone, K L Shepard, and C R Dean. One-dimensional electrical contact to a two-dimensional material. *Science*, 342:614–617, Nov 2013.

[YSYH+14] AF Young, JD Sanchez-Yamagishi, B Hunt, SH Choi, K Watanabe, T Taniguchi, RC Ashoori, and P Jarillo-Herrero. Tunable symmetry breaking and helical edge transport in a graphene quantum spin hall state. *Nature*, 505(7484):528, 2014.

[ZSZ+17] AA Zibrov, EM Spanton, H Zhou, C Kometter, T Taniguchi, K Watanabe, and AF Young. Even denominator fractional quantum hall states at an isospin transition in monolayer graphene. *arXiv preprint arXiv:1712.01968*, 2017.

[ZWO+18] Boyi Zhou, Yiping Wang, Gavin B. Osterhoudt, Paula Lampen-Kelley, David Mandrus, Rui He, Kenneth S. Burch, and Erik A. Henriksen. Possible structural transformation and enhanced magnetic fluctuations in exfoliated α-rucl$_3$. *J. Phys. and Chem. of Solids*, pages 1–5, Jan 2018.